Analysis of Diffraction Grating Induced Distributed Feedback for Stable Single Mode Quantum Cascade Lasers

by

Asif Ahmed

Student ID: 0412062210

A thesis submitted in partial fulfillment

for the degree of **Master of Science**

in the

Department of Electrical and Electronic Engineering

Bangladesh University of Engineering and Technology

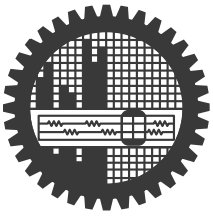

June, 2014

Declaration

It is hereby declared that this thesis or any part of it has not been submitted elsewhere for the award of any degree or diploma.

_____

(**Asif Ahmed**)

Approval Certificate

The thesis titled "Analysis of Diffraction Grating Induced Distributed Feedback for Stable Single Mode Quantum Cascade Lasers" submitted by Asif Ahmed, Student ID: 0412062210, Session: April 2012 has been accepted as satisfactory in partial fulfillment of the requirement for the degree of MASTER OF SCIENCE IN ELECTRICAL AND ELECTRONIC ENGINEERING on June, 2014.

Board of Examiners

1._____ Chairman (Supervisor)

Dr. Muhammad Anisuzzaman Talukder
Associate Professor,
Department of EEE, BUET,
Dhaka-1205, Bangladesh

2._____ Member (Ex-Officio)

Dr. Taifur Ahmed Chowdhury
Professor and Head,
Department of EEE, BUET,
Dhaka-1205, Bangladesh

3._____ Member

Dr. Sharif Mohammad Mominuzzaman
Professor,
Department of EEE, BUET,
Dhaka-1205, Bangladesh

4._____ Member

Dr. Ishtiaque M. Syed
Associate Professor,
Department of Physics,
University of Dhaka

Abstract

Since the first demonstration of quantum cascade lasers (QCLs) in 1994, there has been extensive research on their improvements as QCLs have potential applications in remote chemical sensing and pollution monitoring. By incorporating a distributed feedback (DFB) grating in a QCL structure, single-mode operation with narrower linewidth has been achieved. The coupling coefficient of a DFB-QCL is one of the most important parameters to be considered for manipulating the behavior of the device. In this thesis, we have modeled this parameter using Coupled-Wave theory and observed its dependance on various design parameters such as temperature, grating depth, grating period, tooth angle, duty cycle, and grating shape. It has been found that the value of the coupling coefficient is greatly design-dependent. Since the higher its value, the better the performance of the DFB-QCL to select a single-mode, the design parameters can be changed to obtain a high value of the coupling coefficient. We have also developed a model to obtain the output optical power from a a DFB-QCL. A wide range of operating parameters have been varied to design a stable DFB-QCL for single-mode operation. It has been found that for every design of a DFB-QCL structure, there is an optimum grating depth, grating period and grating shape for which single-mode operation with high value of side-mode suppression ratio (SMSR) is possible.

Acknowledgements

I would first like to thank Almighty Allah for His continuous blessings upon me, especially in my educational life, and for bringing me to the position where I am at this very moment.

My completion of this thesis could not have been accomplished without the ceaseless guidance and support of my thesis supervisor, Dr. Muhammad Anisuzzaman Talukder. He was inspirational in making me come up with the idea of working with distributed feedback quantum cascade laser. During my thesis work, I used the "QCL Simulation Package" developed by him for solving the wavefunctions in quantum cascade lasers. From the very beginning of my thesis work and throughout the last few months, he guided me thoroughly. I consider myself very lucky to have a thesis supervisor like him. And I earnestly hope to maintain an active relation with him for our future research works in the days to come.

Next, I would like to express my gratitude to my teachers and fellow researchers, Golam Md. Imran Hossain, Orchi Hassan, A. F. M. Saniul Haq, Md. Shahadat Hasan Sohel, Fariah Hayee for their continuous support and help for the last one year. I also thank Mehedi Hasan for teaching me the ABC of Lumerical FDTD and MODE Solutions. I am also very grateful to the project HEQEP CP-2091 for letting me use their resources for my simulations.

Finally, my deepest gratitude to my caring, loving, and supportive family. Your encouragement when the times got rough is much appreciated and duly noted.

Contents

List of Figures

List of Tables

Chapter 1

Introduction

The development of lasers has been a turning point in the history of science and engineering. It has produced a completely new type of systems with potentials for applications in a wide variety of fields. Albert Einstein first explained the theory of stimulated emission in 1917, which became the basis of laser. He postulated that when the population inversion exists between upper and lower levels among atomic systems, it is possible to realize amplified stimulated emission and the stimulated emission has the same frequency and phase as the incident radiation. However, it was in the 1950s that scientists and engineers did extensive work to realize a practical device based on the principle of stimulated emission [2]. Since then, they have become ubiquitous, finding utility in thousands of highly varied applications in every section of modern society, including consumer electronics, information technology, science, medicine, industry, law enforcement, entertainment, and the military.

In the early years of the evolution of semiconductor laser, the attention was mainly

focussed on bandgap lasers where the recombination of electron-hole pairs across the semiconductor bandgap results in optical amplification. However, at the end of the 1980s, and beginning of the 1990s, researchers working on resonant tunneling started to work on unipolar laser [3]. In the span of a few years, several proposals appeared on how to achieve population inversion by using intersubband transitions in superlattices or in coupled quantum wells, but none was implemented into a real laser structure [4]. It was only in 1994 that a commercially viable mid-infrared light source versatile enough for a broad range of applications was invented by Faist *et. al.*, who demonstrated a semiconductor injection laser that is built out of semiconductor quantum structures and differs from diode lasers in a fundamental way [5]. In quantum cascade lasers (QCLs), the wavelength is entirely determined by quantum confinement and can be tailored from the mid-infrared to the submillimeter wave region in the same heterostructure material [5].

Modern technologies make extensive and broad use of the electromagnetic spectrum that spans from ultraviolet light through the radio bands. The mid-infrared, nestled within this electromagnetic medium, is very important for sensing a number of gas species like ammonia, benzene, carbon dioxide, carbon monoxide, ethane, formaldehyde, hydrogen sulfide, methane, nitric oxide, nitrous oxide, nitrogen dioxide, sulphur dioxide, and water vapor [6]. The absorption spectra of some of these gases are shown in Fig. 1.1. By using mid-infrared light, scientists within the last decade have developed the ability to detect the presence of specific molecules with unprecedented sensitivity and flexibility.

Within the mid-IR range, a number of environmentally important molecular species

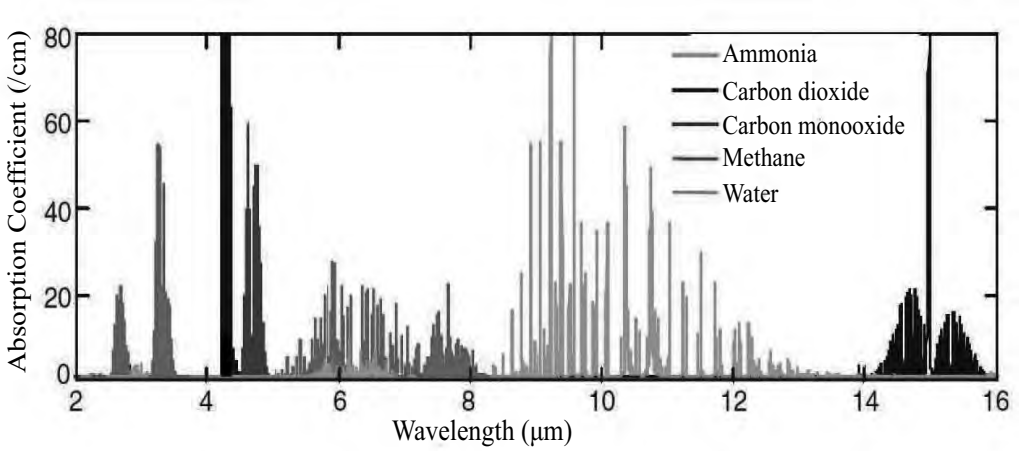

Figure 1.1: Absorption spectra for five gases in the mid IR region of the spectrum (all at 100% vol), taken from the PNNL database [1].

have unique "finger prints" as shown in Fig. 1.1. Whether it is greenhouse gases or toxic chemicals in the workplace, there are many situations where governments, research institutions, and private companies have a need to know "what" and "how much." By detecting if certain wavelengths of light are being absorbed, it can be determined which molecular species exist in a sampled environment and in what quantity, with up to parts per trillion sensitivity. These QCL-based detection systems are compact, portable, and therefore, widely deployable.

Semiconductor diode lasers, including quantum well lasers, rely on transitions between energy bands in which conduction electrons and valence band holes are injected into the active layer through a forward biased p-n junction and radiatively recombine across the material bandgap [7]. However, QCLs rely on only one type of carriers (unipolar semiconductor laser) and on cascading electronic transitions between conduction band states arising from size quantization in semiconductor

heterostructures [8], as schematically shown in Fig. 1.2.

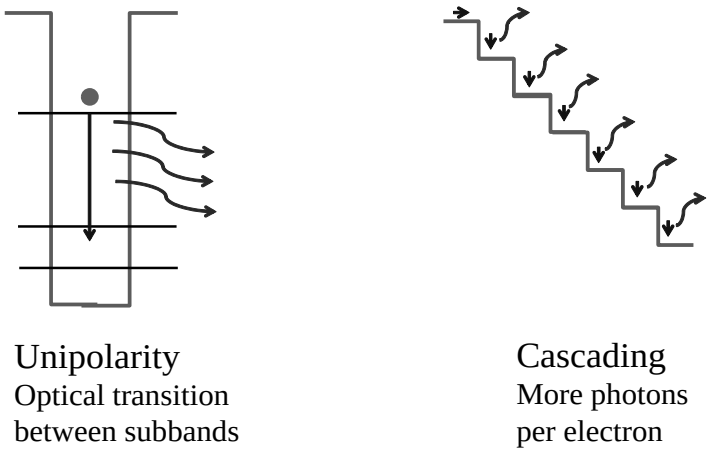

Figure 1.2: Schematic representation of unipolar transition and cascading in a quantum cascade laser.

The unipolarity in QCLs is a consequence of the optical transitions that occur between conduction band states (subbands) arising from size quantization in quantum wells. These transitions are commonly denoted as intersubband transitions. The other fundamental feature of QCLs is the multistage cascade scheme, whereby electrons are recycled from period to period, contributing each time to the gain and the photon emission [8]. In a unipolar QCL, once an electron has undergone an intersubband transition and emitted a photon in one period of the superlattice, it can tunnel into the next period of the structure where another photon can be emitted. This process of a single electron causing the emission of multiple photons as it traverses through the QCL structure gives rise to the name “cascade” and makes a quantum efficiency of greater than unity possible which leads to higher output powers than semiconductor laser diodes.

For most of the applications of QCLs in trace gas sensing, environmental pollution monitoring, and medical diagnostics, they are expected to have a stable single mode emission [9]. The emission spectra of QCLs can be made single mode by processing them as distributed feedback (DFB) lasers [10]. DFB-QCLs use a diffraction grating either buried within or on top of the ridge waveguide to preferentially select a single output wavelength. The attractive feature of single-mode operation of DFB-QCLs have made researchers pursue such devices for the last few years [9, 11, 12, 13].

Since the first report of continuous-wave (CW) operation of Fabry-Perot (FP) QCLs with 3 mW at 312 K around $\lambda \sim 9.1$ μm [14], researchers have been able to demonstrate high CW output powers of several hundred milliwatts at room temperature for FP QCLs [11, 15] through an improved material design, growth quality, and thermal management. However, the output of these FP-QCLs have a multimode emission spectra. As mentioned previously, for many applications, a well-defined single-mode output is desired from a QCL. As a result, room temperature DFB-QCLs have been demonstrated over a wide wavelength range of $3.5-16$ μm [10, 16, 17, 18]. Recently, a pulsed room temperature single mode operation DFB-QCL at a wavelength of 3.34 μm with an output power of 0.8 W has been demonstrated [19]. Recent thermoelectrically (TE) cooled devices provide from hundreds of milliwatt up to watts of CW radiation power from DFB-QCLs [20]. CW DFB-QCLs are increasingly available and combine the advantages of pulsed lasers, such as near room temperature operation and continuously tuneable single mode emission, with straightforward and convenient tuning options [20].

Many groups have employed a number of spectroscopic techniques such as long pass absorption, photoacoustic spectroscopy, cavity ringdown, intracavity absorption, magnetic rotation spectroscopy to monitor a number of molecules of different sizes [21]. Using DFB-QCLs, an ultra-sensitive and selective quartz-enhanced photoacoustic spectroscopy (QEPAS) sensor platform has been demonstrated for detection of carbon monoxide (CO) and nitrous oxide (N_2O) [22]. The development of a sensitive SO_2 QEPAS based sensor platform employing a 140 mW CW-DFB-QCL has also been reported recently [23]. The TE cooled DFB-QCL has been fabricated that emits at ~4.27 μm to detect the presence of SiH_4 [24]. A DFB-QCL array has been demonstrated [25], which achieved single mode lasing coverage of 85 cm^{-1} near 9 μm using a bound-to-continuum active-region design. To demonstrate the applicability of DFB-QCL arrays for remote sensing, the absorption spectrum of isopropanol was measured at a distance of 6 m from the laser array [26].

In DFB-QCLs, the coupling coefficient, κ, is the central parameter, which is a measure of the amount of feedback per unit length provided by the diffraction grating [27]. It is expected to design DFB QCLs with a large κ, so that the coupling strength (κL) that includes the grating length (L), remains large and a shorter device can be used [25]. Also, in order to achieve a single longitudinal mode operation and high-power output, the DFB coupling has to be strong enough to support a single longitudinal mode for the desired laser cavity [9]. A number of design parameters such as the period, duty cycle, tooth angle and depth of the grating, type of cladding material, and temperature can be used to control the value of κ [28, 29]. There have been experimental demonstrations of DFB-QCLs and the

effects of κ on the output characteristics [10, 25, 30]. However, the single mode operation of DFB QCLs is also affected by the operating parameters and a detail theoretical analysis of the dynamics is still lacking. For a successful design and engineering of stable single mode operation of DFB QCLs, a detail theoretical analysis of the diffraction grating and its critical interaction with the laser's gain spectrum is essential. In this thesis, we have performed this analysis by varying the value of κ with various design parameters and its effect on the single-mode operation of the DFB-QCL.

Usually experimental research on DFB-QCLs has been conducted for the analysis of their characteristics [9, 10, 11, 12, 13]. However, with experimental approach, it is difficult to explain the details of the complicated interactions between the electromagnetic wave and the corrugated layer in the top cladding layer of the DFB-QCL. Therefore, it is desirable to establish a theoretical technique for systematically treating wave propagation through a DFB-QCL structure. In this technique, Maxwell's equations are discretized in space and time for the analysis of electromagnetic wave propagation [31] allowing the interaction of the electromagnetic wave and the particles to be traced temporally by the finite-difference time-domain (FDTD) method over time. FDTD is a state-of-the-art method for solving Maxwell's equations in complex geometries [32, 33]. Being a direct time and space solution, it offers a unique insight into all types of problems in electromagnetics and photonics [34]. FDTD technique is not only useful for analyzing the characteristics of the electromagnetic wave in DFB-QCLs, but also can be used as a design tool for performance enhancement of the devices. In this theis, we have used FDTD method for calculating the electric field intensity of output

emission of the QCL and associated optical power with varying wavelength. Using FDTD analysis, we have observed the actual output optical power emitted from the device by varying different design parameters. Thus, from a microscopic analysis of DFB gratings, we have been able to observe the macroscopic effect on DFB-QCLs.

The rest of the thesis is organized as follows:

Chapter 2 focuses on the calculation of the coupling coefficient of DFB-QCLs. Various design parameters such as the period, duty cycle, tooth angle, and depth of the diffraction grating have been varied and their effects on the coupling coefficient have been analyzed.

In Chap. 3, frequency domain solutions have been used to calculate the modes and time-domain solutions have been used to study the dynamics of the distributed feedback of the diffraction grating. The electric field intensity and the output optical power of DFB-QCLs with varying grating period, grating shape, and grating depth have been simulated and single-mode operation has been achieved.

Chapter 4 draws conclusions on the findings of this work. It summarizes the effect of the coupling coefficient on the single mode operation of DFB-QCLs. It also mentions the present technological limitations and future challenges in the performance of the distributed feedback quantum cascade lasers.

Chapter 2

Analysis of Coupling Coefficient of Distributed Feedback Quantum Cascade Laser

2.1 Introduction

To understand the operational characteristic of a DFB-QCL, it is necessary to consider wave propagation in periodic structures. Grating or corrugation-induced dielectric perturbation leads to a coupling between the forward and backward propagating waves. Various approaches like coupled wave theory [27, 35] and Bloch wave analysis [36] have been used to model this coupling behavior. Although these two methods have been proven to be equivalent [37], the coupled wave theory has been accepted widely because numerical algorithms can be implemented to solve the equations in this method, whereas in Bloch wave analysis, several fitting parameters are required for solving the structure that can only be found by

experimental analysis [28].

The coupling coefficient (κ) in a DFB-QCL is a key parameter representing the grating feedback strength in coupled wave theory [29]. It measures the strength of the backward Bragg scattering and thus the amount of feedbcak per unit length provided by the structure. Therefore, the change of κ will have a significant effect on the laser operating characteristics. The coupling coefficient, κ, depends on the operating temperature of the grating as well as on the depth, shape, and duty cycle of the grating. Thus the output characteristics of QCLs can be changed and controlled by varying the operating temperature of the grating as well as the depth, shape, and duty cycle of the grating.

2.2 Coupled Wave Equations

The DFB-QCL has a multi-dielectric stack in which periodic corrugations are formed along one boundary, e. g., in z direction. Within this grating region, perturbation is introduced so that the refractive index and the amplitude gain coefficient become [27, 28]

$$n(z) = n_0 + \Delta n \cos(2\beta_0 z + \Omega) \tag{2.1}$$

and

$$\alpha(z) = \alpha_0 + \Delta\alpha \cos(2\beta_0 z + \Omega + \theta). \tag{2.2}$$

Here, n_0 and α_0 are the steady-state values of the refractive index and amplitude gain, respectively, Δn and $\Delta\alpha$ are the amplitude modulation terms of $n(z)$ and $\alpha(z)$ respectively. The parameter Ω is the non-zero residue phase at the z-axis origin,

β_0 is the Bragg propagation constant so that $\beta_0 = 2\pi n_0/\lambda_B = m\pi/\Lambda$ with m being the order of Bragg diffraction and Λ being the period of the corrugation. The parameter θ is the relative phase difference between perturbations of the refractive index and amplitude gain.

In a semiconductor laser that has a transversely and laterally confined structure, the electric field must satisfy the one-dimensional homogeneous wave equation such that

$$\left[\frac{d^2}{dz^2} + k^2(z)\right] E(z) = 0, \tag{2.3}$$

where the time dependance of the electric field $E(z)$ is $e^{j\omega t}$.

With corrugations extending along the longitudinal direction, the wave propagation constant, $k(z)$, can be written as

$$k^2(z) = \omega^2 \mu \epsilon, \tag{2.4}$$

where ω is the angular frequency and ϵ is the complex permittivity. When the radiation frequency is sufficiently close to the resonance frequency, Eq. (2.4) becomes [7]

$$k^2 = k_0^2 n^2(z)\left(1 + j\frac{2\alpha(z)}{k_0 n(z)}\right), \tag{2.5}$$

where $n(z)$ and $\alpha(z)$ are given by Eqs. (2.1) and (2.2) respectively. It is assumed that the DFB laser oscillates at or near the Bragg wavelength, i. e., $\lambda \approx \lambda_B$, so that the gain is small over distances of the order of a wavelength λ_B, and that the perturbations of the refractive index and the gain are small, i. e., $\Delta n \ll n_0$ and

$\Delta\alpha \ll \alpha_0$. Substituting Eqs. (2.1) and (2.2) into Eq. (2.5) and assuming that $\theta = 0$ generates

$$k^2(z) \approx \beta^2 + 2j\alpha_0\beta + 4\beta\left[\frac{\pi\Delta n}{\lambda} + j\frac{\Delta\alpha}{2}\right]\cos(2\beta_0 z + \Omega), \tag{2.6}$$

where

$$\beta = \frac{2\pi n_0}{\lambda}. \tag{2.7}$$

By collecting all the perturbed terms, one can define a parameter κ [27] such that

$$\kappa = \frac{\pi\Delta n}{\lambda} + j\frac{\Delta\alpha}{2} = \kappa_i + j\kappa_g, \tag{2.8}$$

where κ_i includes all contributions from the refractive index perturbation while κ_g covers all contributions from the gain perturbation.

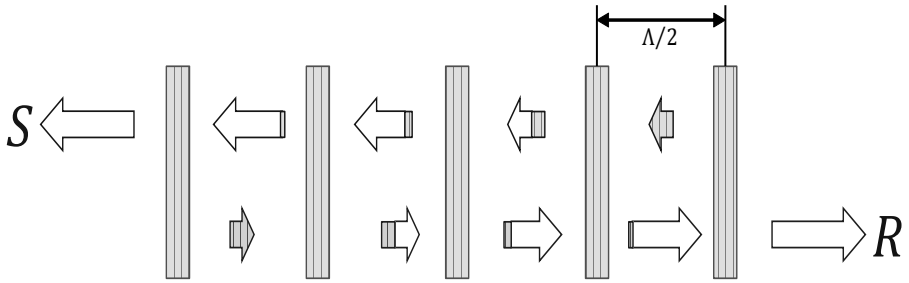

Figure 2.1: Schematic illustration of laser oscillation in a periodic structure.

In Fig. 2.1, we show a simplified illustration which demonstrates the operation of a DFB structure. In the diagram we show two waves represented by arrows, one which travels to the left and the other to the right. As each wave travels in the periodic structure, it receives light at each point along its path by Bragg scattering

from the oppositely traveling wave. This creates a feedback mechanism which is distributed throughout the length of the periodic structure.

If we consider $R(z)$ to be the right traveling wave and $S(z)$ to be the left traveling wave, then following the procedures in [27], we get a pair of coupled wave equations for the DFB-QCL structure such that

$$-\frac{dR}{dz} + (\alpha_0 - j\delta)R = j\kappa_{RS}Se^{-j\Omega}, \tag{2.9}$$

$$\frac{dS}{dz} + (\alpha_0 - j\delta)S = j\kappa_{SR}Re^{j\Omega}, \tag{2.10}$$

where

$$\kappa_{RS} = \kappa_i + j\kappa_g e^{-j\theta} \tag{2.11}$$

is the general form known as the forward coupling coefficient [38], and

$$\kappa_{SR} = \kappa_i + j\kappa_g e^{j\theta} \tag{2.12}$$

is the backward coupling coefficient.

2.3 QCL Gain Medium

The QCL structure that we have used has an active region based on a bound-to-continuum design [39]. The bound-to-continuum approach provides a high population inversion and low-threshold current densities even at high temperatures [39]. In this design the active region spans the whole period and consists of a chirped superlattice presenting a tilted lower miniband whose width is maximum

in the center and decreases on both sides close to the injection barriers. The upper state is created in the first minigap by a small well adjacent to the injection barrier. Its wavefunction has a maximum close to the injection barrier and decreases smoothly in the active region. This upper state is well separated from the higher-lying states of the superlattice, lying in its first minigap. It therefore does not need to be confined by separating the structure into an active region and an injection/relaxation region.

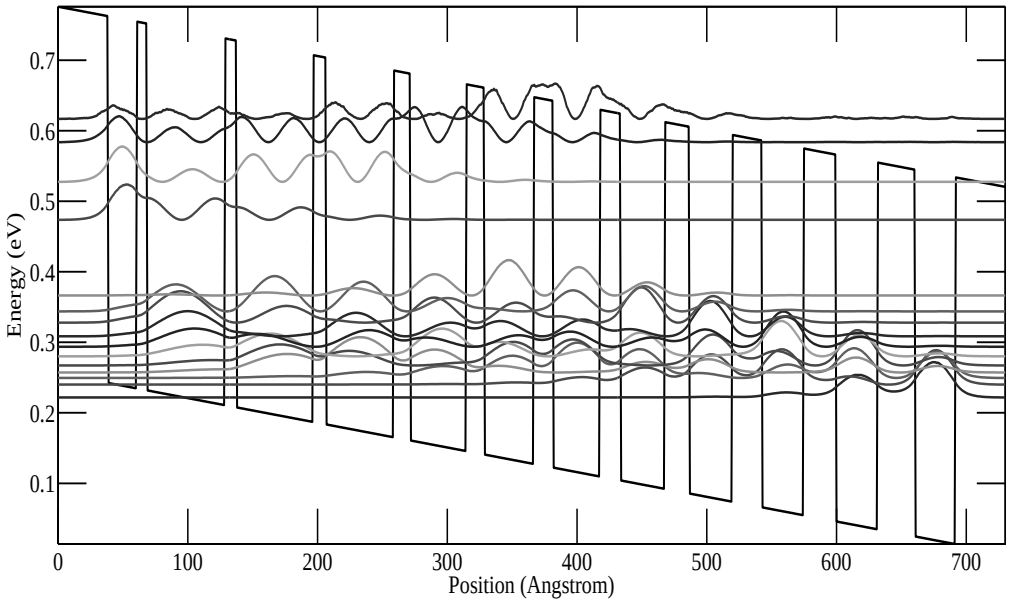

Figure 2.2: Band structure and the relevant moduli squared wave functions for active/injector region under an applied electric field of 35 kV/cm and 200 K temperature. The layer sequence of a period of the structure, is **3.9/** 2.2/ **0.8**/6/ **0.9/** 5.9/**1**/5.2/ **1.3/** 4.3/**1.4**/3.8/**1.5**/3.6/ **1.6/** 3.4/**1.9/** 3.3/ **2.3/** 3.2/**2.5/** 3.2/**2.9**/3.1, where the layer sequences are given in nm, $In_{0.52}Al_{0.48}As$ barriers are in bold face, $In_{0.53}Ga_{0.47}As$ wells are in normal face, and numbers underlined correspond to the n-doped layers (Si, $2.3 \times 10^{17}\,cm^{-3}$).

The QCL gain medium that we have used is based on the works mentioned in [40].

It uses alternate layers of $In_{0.52}Al_{0.48}As$ and $In_{0.53}Ga_{0.47}As$ layers. It is designed to emit light in the 9 μm range. The conduction band diagram of one stage is shown schematically in Fig. 2.2 with the computed relevant wavefunctions.

2.4 Waveguide Structure

The first step in processing quantum cascade gain material to make a useful light-emitting device is to confine the gain medium in an optical waveguide. This makes it possible to direct the emitted light into a collimated beam, and allows a laser resonator to be built such that light can be coupled back into the gain medium.

Two types of optical waveguides are in common use. A ridge waveguide is created by etching parallel trenches in the quantum cascade gain material to create an isolated stripe of QC material as shown in Fig. 2.3(a). A dielectric material is typically deposited in the trenches to guide injected current into the ridge, then the entire ridge is typically coated with gold to provide electrical contact and to help remove heat from the ridge when it is producing light. Light is emitted from the cleaved ends of the waveguide.

The second waveguide type is a buried heterostructure as shown in Fig. 2.3(b). Here, the QC material is also etched to produce an isolated ridge. Now, however, new semiconductor material is grown over the ridge. The change in index of refraction between the QC material and the overgrown material is sufficient to create a waveguide. Dielectric material is also deposited on the overgrown material

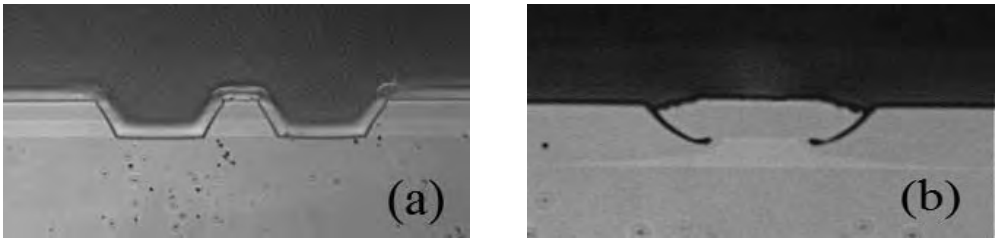

Figure 2.3: (a) End view of QC facet with ridge waveguide. Darker gray: InP, lighter gray: QC layers, black: dielectric, gold: Au coating, (b) End view of QC facet with buried heterostructure waveguide. Darker gray: InP, lighter gray: QC layers, black: dielectric.

around QC ridge to guide the injected current into the QC gain medium. Buried heterostructure waveguides are efficient at removing heat from the QC active area when light is being produced.

Our design is based on a first-order DFB of rectangular shape that is formed in the upper waveguide cladding of the QCL [25]. It is designed as an etched corrugation in a buried InGaAs layer just above the active region of the laser as shown in Fig. 2.4. Referring to Fig. 2.4, the DFB-QCL structure consists of a bottom waveguide cladding of 4 μm of InP doped $1 \times 10^{17}\text{cm}^{-3}$ (red), followed by 580 nm of InGaAs doped $3 \times 10^{16}\text{cm}^{-3}$ (yellow), a 2.4 μm thick lattice-matched active region (blue), 580 nm of InGaAs doped $3 \times 10^{16}\text{cm}^{-3}$ where the grating is etched 500 nm deep (yellow), and a top waveguide cladding of 4 μm InP doped $1 \times 10^{17}\text{cm}^{-3}$ (red). The active region consists of 35 stages based on a bound-to-continuum design as described in Sec. 2.3. The period of the grating is 1.4 μm.

This type of structure is known as purely index-coupled DFB, where coupling is solely generated by the refractive index perturbation [41]. Since most carrier tran-

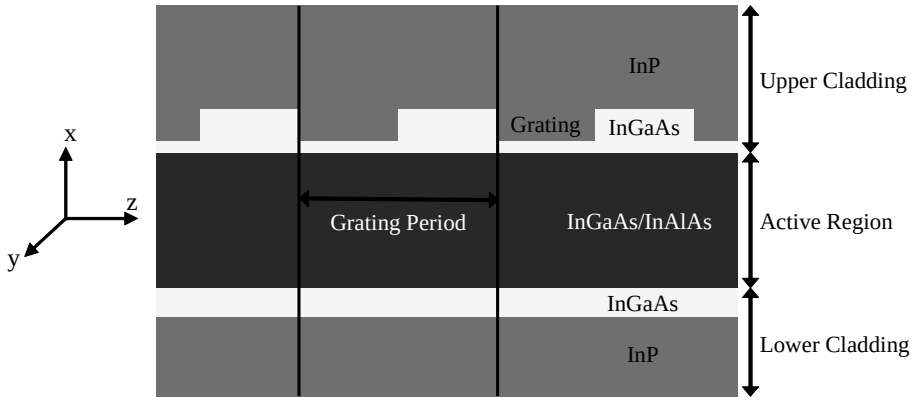

Figure 2.4: Schematic illustration of the DFB-QCL waveguide with rectangular grating. The grating is etched in InGaAs layer (yellow) in the top waveguide cladding, just above the active region (blue). An InP layer is overgrown on top of the grating (red).

sition is confined along the active layer, the amplitude gain of the DFB-QCL will not be affected. Therefore, with $\kappa_g = 0$, the index coupling coefficient κ_i, which is purely real, is related to κ_{RS} and κ_{SR} by the following expression [28]

$$\kappa_{RS} = \kappa_{SR} = \kappa_i. \tag{2.13}$$

Therefore, the expression of the coupling coefficient for a DFB-QCL reduces to

$$\kappa = \frac{\pi \Delta n}{\lambda} = \kappa_i. \tag{2.14}$$

There can be two other types of DFB-QCL waveguide. In a mixed-coupled DFB, due to the variation of refractive index along the corrugation layer, index coupling is induced. Also, the active layer thickness becomes a periodic function along the longitudinal direction and so it modifies the amplitude gain along that direction.

Thus, gain coupling is induced. This type of structure is shown in Fig. 2.5(a).

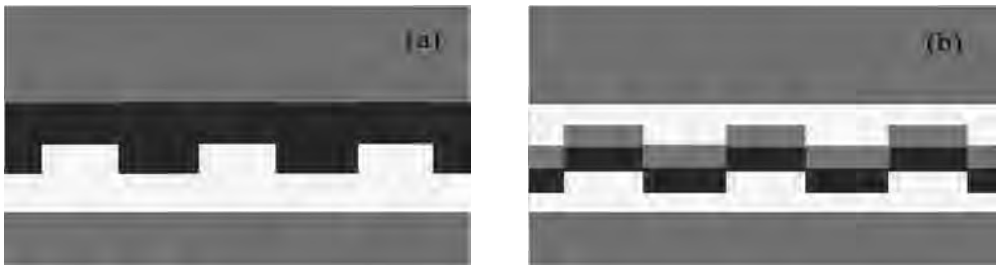

Figure 2.5: Simplified schematic diagrams showing (a) a mixed-coupled DFB-QCL and (b) a purely gain-coupled DFB-QCL.

The other type of DFB grating id gain-coupled or loss-coupled DFB as shown in Fig. 2.5(b). In this case, the second corrugation demonstrates an inverse corrugation phase with respect to the first layer of grating. Thus, the effect of index coupling can be canceled out.

We note that although the gain-coupled DFB lasers have attracted considerable interest because of smaller sensitivity to external reflection [42, 43], their weak optical confinement limits the beam quality [44]. Moreover, it is difficult to obtain a stable output in single longitudinal mode. As a result, the index-guiding mechanism has become the mainstream in semiconductor laser development and a large number of index-guided structures have been proposed [41], where a lateral variation of refractive indices is used to confine the optical energy.

We have also analyzed a DFB-QCL structure with a layer of trapezoidal corrugation. Although the rectangular grating DFB-QCLs are better for single-mode operation, trapezoidal gratings are important since fabrication processes are more

likely to build trapezoidal gratings rather than rectangular ones [45]. The schematic illustration of the structure is shown in Sec. 2.6.4 with the results obtained from such structure.

The DFB grating gives rise to a photonic band gap (PBG). PBG is a term applicable to dielectric media which possess alternate regions of low and high refractive index such that the transmission of photons or light energy of certain frequencies is forbidden. Thus it is a photon forbidden region analogous to electron forbidden region in the case of electron band gap of semiconductors. The DFB supports lasing for longitudinal modes on either side of this gap. There are two modes that are directly at either edge of the photonic gap as schmeatically shown in Fig. 2.6. In the higher index part of the grating the low-frequency mode is more concentrated and in the lower index part of the grating the high-frequency mode is more concentrated.

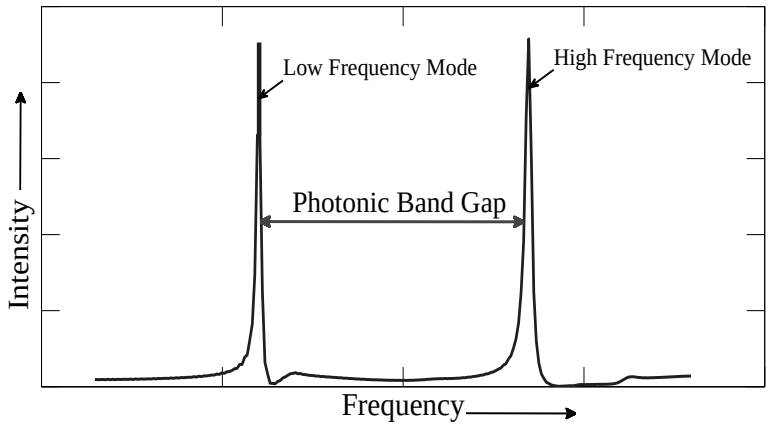

Figure 2.6: Schematic illustration of the photonic band gap created inside a DFB-QCL.

The coupling coefficient (κ) of the grating is usually a complex number. Its real part corresponds to the refractive index perturbation and proportional to the photonic gap. Its imaginary part corresponds to the gain (or loss) perturbation. The modes can be simulated numerically to find κ using Eq. (2.15) and expanding into

$$\kappa = \frac{\pi \Delta n}{\lambda} = \frac{\pi (n_1 - n_2)}{\lambda}. \tag{2.15}$$

Here, n_1 is the modal effective refractive index of the higher index part of the grating, i. e., InGaAs layer and n_2 is the modal effective refractive index of the lower index part of the grating, i. e., InP layer. These two values of refractive indices are obtained from Lumerical MODE Solutions software where the refractive indices of core and cladding layers are given as input.

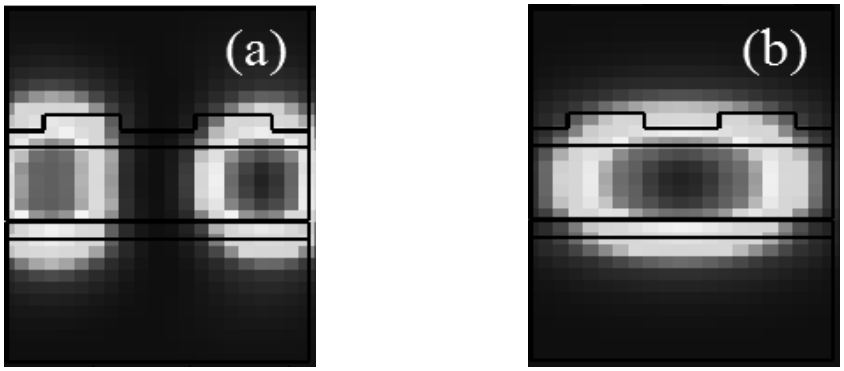

Figure 2.7: Mode simulation of the mode on the (a) low frequency side and (b) high frequency side of the photonic gap of the DFB grating. The plots display the magnitude of the electric field in the laser structure.

Figures 2.7(a) and (b) show the mode profile calculated for the low and high frequency DFB modes, for two periods of the grating. In the grating structure, the part that is indented down has a lower effective refractive index than the part that

is raised up. As previously mentioned, the low-frequency mode is more concentrated in the higher index part of the grating and the high-frequency mode is more concentrated in the lower index part of the grating.

2.5 Calculation of Refractive Indices

2.5.1 Active Region

We take the weighted average of the refractive indices of the materials of the well and barrier of the hetero-structure to calculate the index of refraction of the active region which is also the core of our waveguide structure. If n_1 and n_2 are the refractive indices of the well and the barrier materials, respectively, and x_1 and x_2 are the thicknesses of the well and the barrier materials, respectively, the index of refraction of the active region can be calculated by

$$n_{\text{active}} = \frac{\sum n_1 x_1 + \sum n_2 x_2}{\sum x_1 + \sum x_2}. \tag{2.16}$$

The refractive indices of the well and barrier material (n_1 and n_2 respectively) have been modeled using the Ravindra relation [46], which is an approximation of the Penn model [47] and is given by

$$n = 4.16 - 1.12E_g + 0.31E_g^2 - 0.08E_g^3. \tag{2.17}$$

Here, E_g is the bandgap of the material that can be calculated using the model of Varshni [48] as

$$E_g = E_{g,0} - \frac{\alpha T^2}{\beta + T}, \tag{2.18}$$

where $E_{g,0}$ is the bandgap at 0 K temperature, α and β are fitting parameters characteristics of a given material.

In the case of alloy materials, the temperature-dependent bandgaps of the constituents, E_g^A and E_g^B, are calculated by Eq. (2.18). However, for materials where the bandgap changes between direct and indirect, the multiple valley conduction bands are considered. For that purpose, additional model parameters are needed for the higher energy valleys in the respective III-V binary materials.

The bandgap and the energy offset of an alloy $A_{1-x}B_x$ are calculated by

$$E_{g,X}^{AB} = E_{g,X}^{A}(1-x) + E_{g,X}^{B}x + C_{g,X}(1-x)x, \tag{2.19}$$

$$E_{g,\Gamma}^{AB} = E_{g,\Gamma}^{A}(1-x) + E_{g,\Gamma}^{B}x + C_{g,\Gamma}(1-x)x, \tag{2.20}$$

$$E_{g}^{AB} = min(E_{g,X}^{AB}, E_{g,\Gamma}^{AB}). \tag{2.21}$$

The above mentioned parameters are given in Table 2.1. The bowing parameters $C_{g,X}$ and $C_{g,\Gamma}$ are summarized in Table 2.2.

2.5.2 InP Layer

The InP layer in the top and bottom waveguide cladding of the waveguide in Fig. 2.4 is a doped layer. The model of the refractive index of InP described in Sec. 2.5.1 is based on undoped InP. Therefore, we need a different refractive index model for InP to incorporate doping.

Table 2.1: Values of $E_{g,0}$, α and β for different materials

Material	**Minimum**	$E_{g,0}$ **(eV)**	α **(eV/K)**	β **(K)**	**References**
GaAs	Γ	1.521	5.58×10^{-4}	220	[49]
GaAs	X	1.981	4.6×10^{-4}	204	[50]
AlAs	Γ	2.891	8.78×10^{-4}	332	[50]
AlAs	X	2.239	6×10^{-4}	408	[51]
InAs	Γ	0.420	2.5×10^{-4}	75	[52]
InAs	X	2.278	5.78×10^{-4}	83	[50]

Table 2.2: Values of $C_{g,\Gamma}$ and $C_{g,X}$ for different materials

Material	$C_{g,\Gamma}$ **(eV)**	$C_{g,X}$ **(eV)**	**References**
InGaAs	-0.475	-0.475	[51]
InAlAs	-0.3	-0.713	[51]

Pettit *et al.* proposed a Sellmeier formula for InP doped with $N = 5 \times 10^{16}\text{cm}^{-3}$ that relates refractive index with wavelength [53]. The proposed relation is given by,

$$n^2 = 7.255 + \frac{2.316\lambda^2}{\lambda^2 - 0.392 \times 10^6}, \tag{2.22}$$

where λ is in nm. The validity of Eq. (2.22) can be extended to InP materials exhibiting a doping level lower than 10^{18}cm^{-3} [54]. Following the work in [53], Martin *et al.* proposed a similar Sellmeier formula that was obtained as the best-fit of their measured data and given as [55]

$$n^2 = 7.194 + \frac{2.282\lambda^2}{\lambda^2 - 0.422 \times 10^6}, \tag{2.23}$$

where λ is in nm. Equation (2.23) applies to $N = 2 \times 10^{18}\text{cm}^{-3}$ doped InP. Equations (2.22) and (2.23) are particular for two different doping concentrations and have a similar behavior with wavelength. Therefore, we can interpolate the value of refractive index of InP for a different doping concentration from these two curves using linear curve fitting technique.

2.5.3 InGaAs Layer

As in the case of InP layer mentioned in Sec. 2.5.2, the InGaAs layer in the top and bottom waveguide cladding of the waveguide in Fig. 2.4 is also a doped layer. The model of the refractive index of InGaAs described in Sec. 2.5.1 is based on undoped InGaAs. To calculate the effect of doping concentration on the refractive index of InGaAs, we take similar approach as in the case of InP and use the results obtained by Gozu *et al.* [56]. Using the Sellmeier equation for GaAs they

proposed a simple model based on the shift of the band gap energy $E_g(x)$ of the $In_xGa_{1-x}As$ alloy given by

$$n^2 = 8.95 + \frac{2.054}{1 - \left[0.6245 \frac{1.424}{\lambda E_g(x)}\right]^2}, \tag{2.24}$$

with

$$E_g(x) = 1.424 - 1.501x + 0.436x^2, \tag{2.25}$$

where x is the In content in $In_xGa_{1-x}As$.

2.6 Effects of Different Parameters on κ

Since the coupling coefficient is associated with the perturbed relative permittivity, the numerical value of κ depends on the shape, depth, duty cycle and period of the corrugation. In addition, as the temperature changes the refractive indices, it may also affect the coupling coefficient.

2.6.1 Variation of Duty Cycle of Grating

The duty cycle of the grating is defined as the ratio of the groove to the total length of groove and ridge. The DFB-QCL waveguide structure of Fig. 2.4 has been analyzed to determine the coupling coefficient with varying duty cycle. We have varied the grating periods between 1.3 and 1.5 μm with 0.1 μm increment, satisfying the Bragg condition for lasing wavelengths between 8.5 and 9.6 μm, with an effective refractive index of 3.27 as calculated in our mode simulations. The grating depth is 500 nm and the temperature is 200 K. The result is shown in

Fig. 2.8.

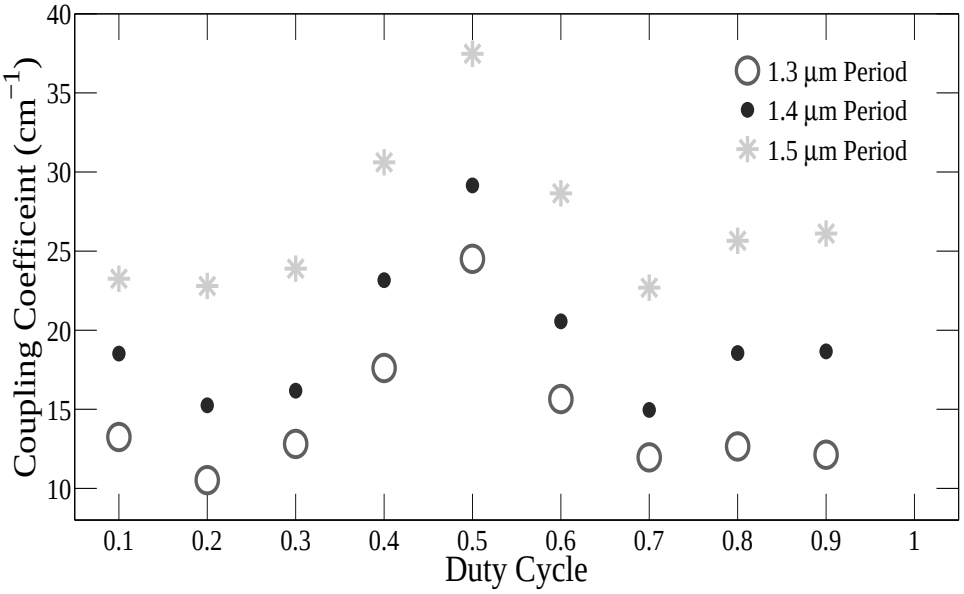

Figure 2.8: Dependence of Coupling Coefficient on Duty Cycle of the waveguide of Fig. 2.4.

As can be seen from Fig. 2.8, the value of the coupling coefficient shows a maxima at 50% duty cycle and decreases as the duty cycle is made higher or lower to this value. This is coherent with the result found by Millett *et al.* [57]. A 50% duty cycle maximizes the refractive index contrast [25]. This means the wave propagating through the length of the structure is incident on equal length of InP and InGaAs layer. Therefore, the difference of the refractive indices gets maximum and we get the highest value of κ. If we increase or decrease the duty cycle, the length of either the InP layer or the InGaAs layer increase with respect to the other. This minimizes the refractive index contrast and thus κ decreases.

2.6.2 Variation of Grating Depth

The grating coupling coefficient per unit length has also been calculated for varying grating depth for the waveguide structure of Fig. 2.4. As in the variation of κ with duty cycle in Sec. 2.6.1, the period of the grating is varied between 1.3 and 1.5 μm with 0.1 μm increment. The duty cycle is 0.5 and the temperature is 200 K. The results are shown in Fig. 2.9.

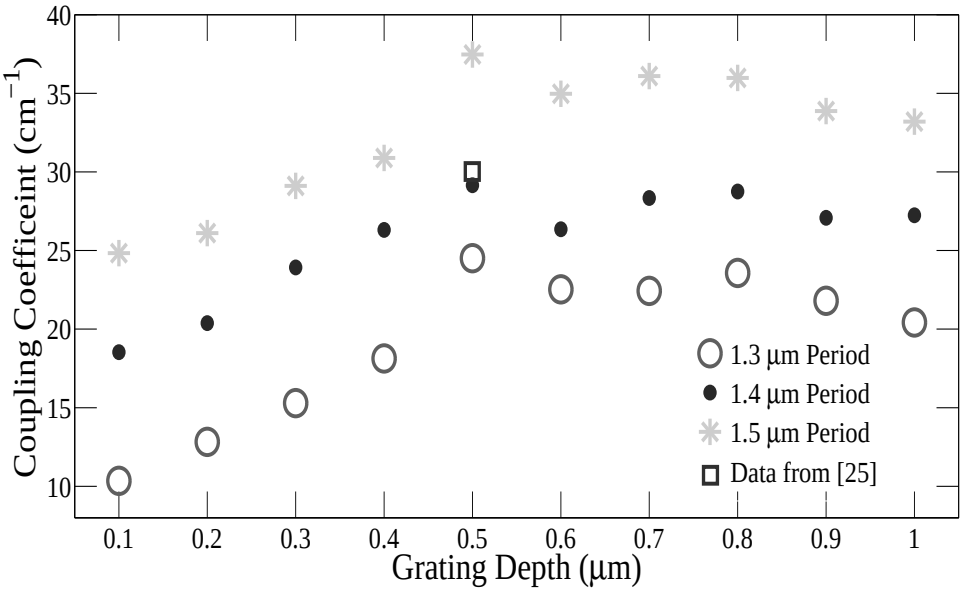

Figure 2.9: Dependence of Coupling Coefficient on the Grating Depth of the waveguide of Fig. 2.4.

It is evident from Fig. 2.9 that for a grating period of 1.4 μm, with increasing grating depth, coupling coefficient reaches a maximum of 29.15 cm^{-1} for a grating depth of 500 nm. Lee *et. al.* fabricated a DFB-QCL waveguide structure of Fig. 2.4 for a grating depth of 500 nm and from their experimental data they found a coupling coefficient of $\sim$ 30 cm^{-1} [25], which shows only $\sim$ 2% deviation from

our result. Thus, we can say that our model for the calculation of the coupling coefficient is fairly accurate. We can see that increasing grating depth beyond this value has little effect on κ. With shallower gratings, there is less amount of refractive index contrast, so the value of κ is smaller. This is particular for the waveguide structure of Fig. 2.4. Although a deeper grating would be beneficial in maximizing the reflectivity [58], it would minimize the side-mode suppression ratio [59] and maximize the spectral width of the gain spectrum, which in turn would create a multi-mode laser instead of a single mode. Therefore, a grating depth of 500 nm has been chosen for the waveguide of Fig. 2.4 as a trade-off between these two effects.

2.6.3 Variation of Grating Tooth Angle

To observe the dependence of the coupling coefficient on the shape of the grating tooth, it has been calculated by varying the tooth sidewall angle of the waveguide. A 90° angle results in rectangular grating as shown in the waveguide of Fig. 2.4 and an angle less than 90° results in trapezoidal grating as shown in the waveguide of Fig. 2.11. The grating angle has been varied from 60° to 90° for 1.3, 1.4, and 1.5 μm. The grating depth is 500 nm and the temperature is 200 K. The result is shown in Fig. 2.10.

As shown in Fig. 2.10, the value of κ is largest for rectangular grating with 90° tooth angle. However, trapezoidal grating with lower tooth angle is still of interest since it has been shown that the maximum reflectance of the waveguide mode is attained using a trapezoidal grating [60]. Also, the top and bottom width of the

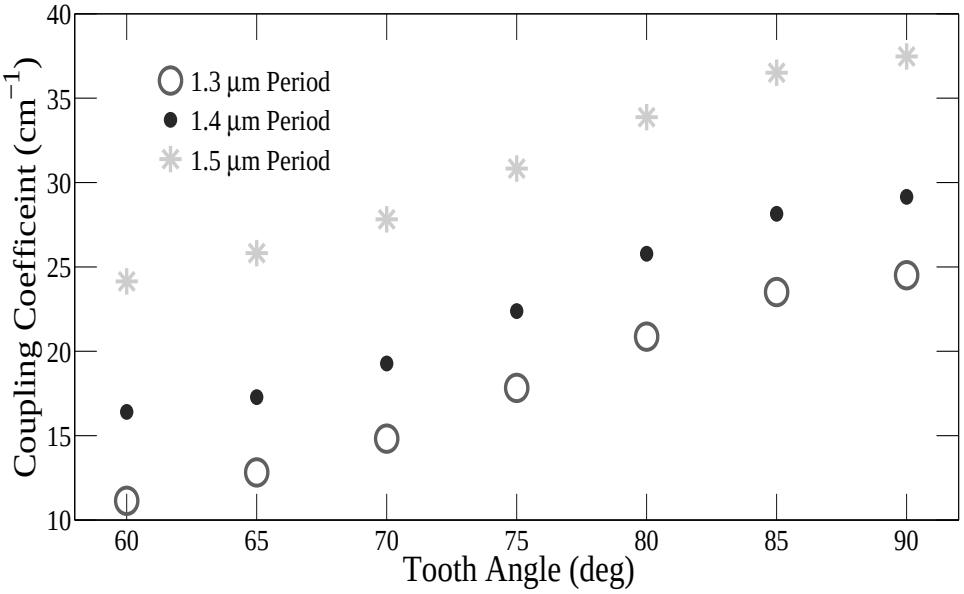

Figure 2.10: Dependence of Coupling Coefficient on the Grating Tooth Angle of the waveguide of Fig. 2.4.

grating (W_T and W_B, respectively, in Fig. 2.11) can be changed to get a maximum value of the coupling coefficient. This effect has been presented in detail in Sec. 2.6.4.

2.6.4 Coupling Coefficient for Trapezoidal Corrugation

The fabrication of gratings by dry etching techniques results in a trapezoidal shape and the wall angle can be modified by the ion incident angle [45]. In this section, the coupling coefficient values based on the five-layer DFB waveguide with trapezoidal grating, as shown in Fig. 2.11, will be investigated. The structural parameters as defined in Fig. 2.11 are listed in Table 2.3.

As explained for rectangular corrugation, since the active layer thickness remains

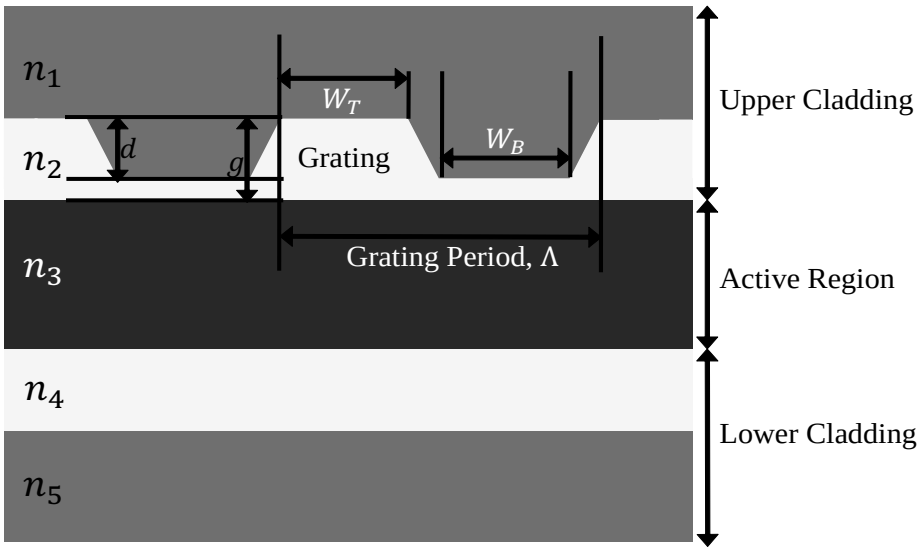

Figure 2.11: Schematic illustration of the DFB-QCL waveguide with trapezoidal grating. The grating is etched in InGaAs layer (yellow) in the top waveguide cladding, just above the active region (blue). An InP layer is overgrown on top of the grating (red).

constant along the longitudinal direction, any gain or loss coupling can be neglected and only pure index coupling exists in the case of trapezoidal corrugation.

By setting $m = 1$ in $\beta_0 = m\pi/\Lambda$, the coupling coefficient of the first-order trapezoidal corrugation has been determined following the method described in [41]. We have studied the effects of different corrugation shapes on the coupling coefficient and the results are illustrated in Fig. 2.12. The results are similar with those found by Ghafouri-Shiraz *et. al.* [61].

In Fig. 2.12, the coupling coefficient is plotted against the bottom width of corrugation (W_B), while different values of the top width of corrugation (W_T) have been used as a comparison. Both W_B and W_T are normalized with respect to the

Table 2.3: Structural parameters used in determining κ of the first-order trapezoidal corrugation

Parameter	**Value**
m	1
d	580 nm
g	500 nm
$n_1 = n_5$	3.11
$n_2 = n_4$	3.2
n_3	3.27

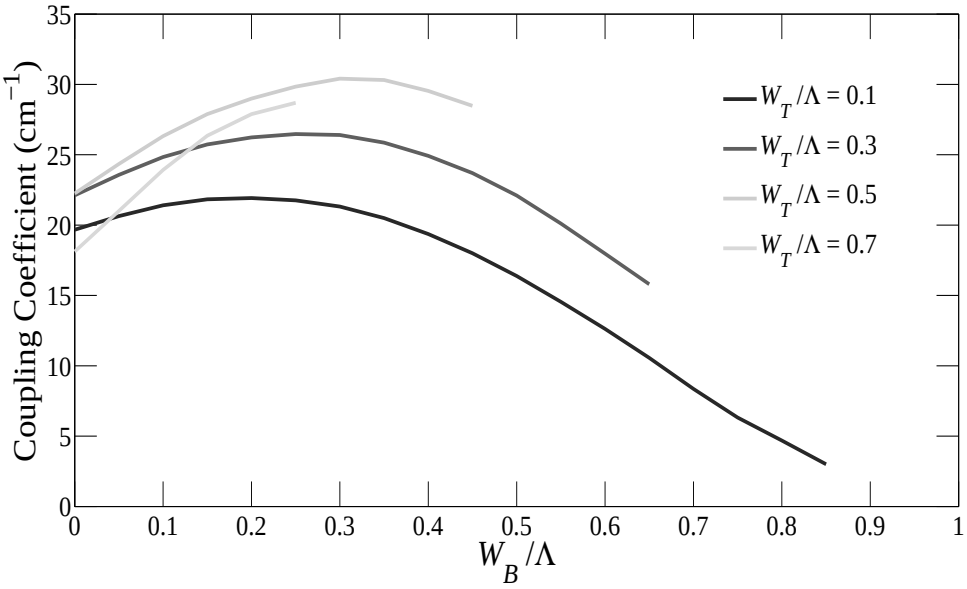

Figure 2.12: The change in the first-order coupling coefficient with W_B/Λ for different values of W_T/Λ.

corrugation period (Λ). As observed in Fig. 2.12, there exists a peak coupling coefficient where the largest possible optical feedback can be achieved. With the normalized top width W_T/Λ increasing from 0.1 to 0.7, the associated W_B/Λ values of the peak coupling coefficient also increase.

The similar analysis has been done for second-order Bragg diffraction. The parameters used to determine the coupling coefficient of the second-order trapezoidal corrugation can be found in Table 2.4.

Table 2.4: Structural parameters used in determining κ of the second-order trapezoidal corrugation

Parameter	**Value**
m	2
d	1080 nm
g	1000 nm
$n_1 = n_5$	3.11
$n_2 = n_4$	3.2
n_3	3.27

The effect of corrugation shapes on the second-order coupling coefficient has been investigated in Fig. 2.13.

Just as for the first-order plot shown in Fig. 2.12, the coupling coefficient is shown as a function of W_B/Λ for various values of W_T/Λ. As observed in Fig. 2.13, there exist two peak values of coupling coefficients along the W_B/Λ axis for each

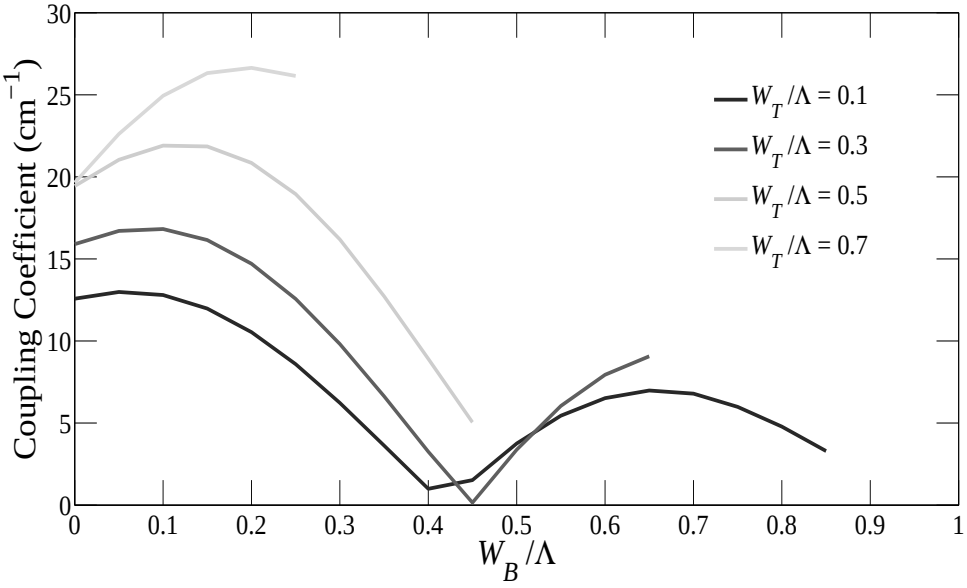

Figure 2.13: The change in the second-order coupling coefficient with W_B/Λ for different values of W_T/Λ.

selected value of W_T/Λ. In between the peaks, there are places where the coupling coefficient drops to almost zero value. This may happen because the electric field diffracted by the second-order corrugation is completely out of phase with the incident wave. Therefore, zero coupling coefficients follow at that particular corrugation shape.

2.6.5 Variation of Temperature

We have analyzed the DFB-QCL waveguide structure of Fig. 2.4 to determine the coupling coefficient with varying temperature. The period of the grating is 1.4 μm, the depth is 500 nm and the duty cycle is chosen to be 50%, which is typical of first-order DFBs, as this maximizes the refractive index contrast [25]. The variation of refractive index of the active layer with temperature is shown in Fig. 2.14.

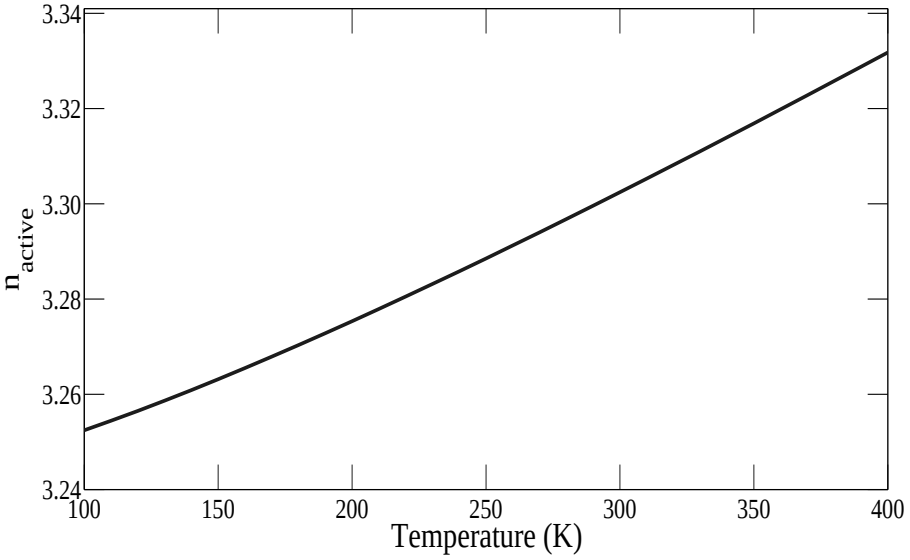

Figure 2.14: Index of refraction of active region vs. temperature.

As can be seen from Fig. 2.14, the refractive index tends to increase with increasing temperature. This can be explained by considering impurity levels and interfacial defects. At high temperature, these effects dominate and linewidth increases due to a larger energy spread of the carrier distribution and phonon scattering [62]. Also, the electron wavefunctions at impurity levels may generate a narrow impurity band extending into the conduction band and reducing effective bandgap [63]. As a result, the index of refraction increases.

The variation of refractive indices of InP and InGaAs cladding layers with temperature are also shown in Fig. 2.15. We note that the refractive index of InP cladding layer is essentially constant with the changing temperature. This is due to the fact that the refractive index of InP has been modeled assuming that it depends only

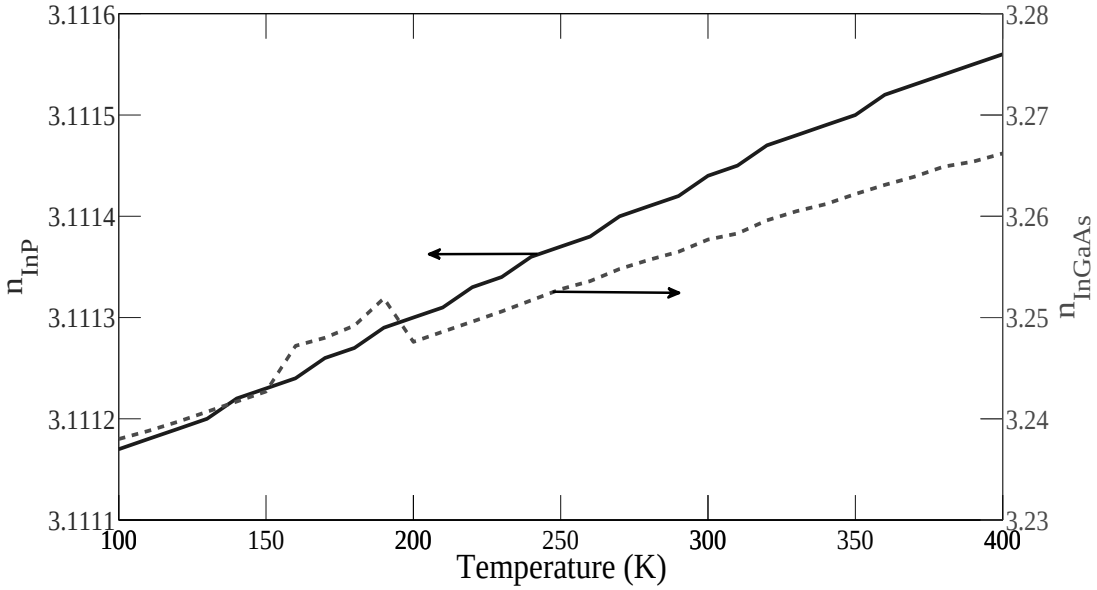

Figure 2.15: Index of Refraction vs. Temperature of the InP and the InGaAs cladding layer.

on the doping concentration and emission wavelength as described in Sec. 2.5.2. The model is based on the works of Pettit *et al.* [53] and Martin *et al.* [55] where temperature has not been considered as an affecting parameter. Therefore, we do not notice significant changes in the value of refractive indices of InP and InGaAs layer with changing temperature. However, there is an increase in the refractive index of InGaAs in the 160 K to 190 K temperature range that affects the coupling coefficient value as will be shown in 2.16.

The variation of the coupling coefficient of the waveguide structure of Fig. 2.4 with temperature is shown in Fig. 2.16. MATLAB and Lumerical MODE Solutions have been used to determine the coupling coefficient, the details of which are given in Appendix A.

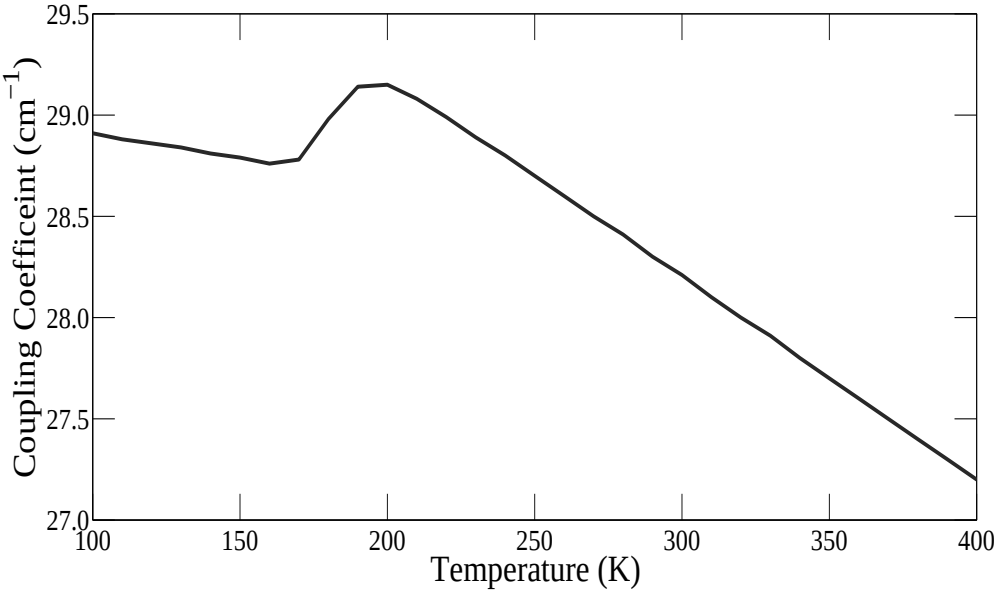

Figure 2.16: Dependence of Coupling Coefficient on Temperature of the waveguide of Fig. 2.4.

The coupling coefficient decreases with increasing temperature. The value is well matched with that determined by Lee *et al.* [25]. The higher the temperature, the lower the coupling coefficient, and the lower the strength of the backward Bragg scattering and consequently, lower amount of feedback provided by the structure. However, there is a slight increase in the value of κ in the 160 K to 190 K temperature change. This corresponds to the increase of refractive index of InGaAs layer in the same temperature range that results into larger difference in the refractive indices of the modes (Eq. (2.15)) and a larger value of κ.

2.7 Summary

In this chapter, the analysis of the coupling coefficient (κ) of distributed feedback quantum cascade laser has been performed. The key points found in this chapter have been summarized here:

- The value of κ is maximum for 50% duty cycle of the corrugation of our structure. This helps to maximize the refractive index contrast and also the fabrication of the device gets easier.
- As the grating depth is increased, the value of κ for our chosen structure first increases and after a depth of 500 nm, the change in its value is not substantial.
- With increasing grating period, the value of κ increases.
- The value of κ increases with increasing tooth angle of the grating. It is highest for rectangular corrugation with a tooth angle of 90°.
- The effect of trapezoidal grating in DFB-QCL waveguide structure has been analyzed with changing the top and bottom width of the corrugation. The value of κ reaches a maximum value for a particular value of the top and bottom width of corrugation. This has been analyzed for both first-order and second-order coupling coefficient.
- With increasing temperature, the value of κ decreases. This results into lower amount of feedback from the corrugation degrading its performance as a single-mode lasing source. For the QCL structure discussed in Sec. 2.3

and waveguide structure discussed in Sec. 2.4, it has been found that the value of κ is maximum at 200 K.

Following the results found in this chapter, the waveguide structure of Sec. 2.4 has been used in analyzing the output characteristics of the DFB-QCL with 200 K temperature, 50% duty cycle, various grating depth, both rectangular and trapezoidal corrugation and three different grating periods.

Chapter 3

Single Mode Operation of Distributed Feedback Quantum Cascade Laser

3.1 Introduction

DFB laser diodes do not use two discrete mirrors to form the optical cavity (as they are used in conventional laser designs). The grating acts as the wavelength selective element for at least one of the mirrors and provides the feedback, reflecting light back into the cavity to form the resonator. The grating is constructed so as to reflect only a narrow band of wavelengths, and thus produce a single longitudinal lasing mode. This is in contrast to a Fabry-Perot Laser, where the facets of the chip form the two mirrors and provide the feedback. In that case, the mirrors are broadband and either the laser functions at multiple longitudinal modes simultaneously or easily jumps between longitudinal modes. In this chapter, we

first discuss about the gain spectrum and the oscillating modes of the QCL. Next, we present a detailed description of our computational model for simulating the output characteristics of the DFB-QCL. Finally, we present our analytical results.

3.2 Gain Spectrum

To analyze the effect of grating structure (in the upper cladding of the waveguide) on the output emission wavelength and how it affects the performance of a quantum cascade laser, we have focussed our attention on the gain of the lasing medium and the modes of the output emission. In general, the gain in a laser refers to the light produced by stimulated emission of photons. For photon generation population inversion is a necessary condition. It refers to a state where the carrier population density in upper lasing level of the laser is more than the lower lasing level. Lasing levels are the discrete energy levels created by the quantum well structures in the conduction band. Some of the photons generated by electron transitions get absorbed in lasing medium and at the two mirrors by various processes. To get sufficient light output the gain co-efficient must be large enough to overcome the different losses in the laser.

3.2.1 Gain

The peak modal gain between two sub-bands i and j assuming Lorentzian lineshape is given by [64]

$$G_m = G_p \Gamma, \tag{3.1}$$

where G_p is the peak material gain between sub-bands i and j, and is given by

$$G_p = \frac{4\pi q^2}{\epsilon_o n \lambda_o} \frac{z_{ij}^2}{2\gamma_{ij} L_p} (N_i - N_j). \tag{3.2}$$

Here, q is the charge of an electron, ϵ_o is the permittivity of free space, n is the effective refractive index of laser, λ_o is the photon wavelength, $2\gamma_{ij}$ is the linewidth (FWHM) of QCL, L_p is the length of active region of QCL, z_{ij} is the dipole matrix element, N_i is the sheet electron density in upper lasing level i and N_j is the sheet electron density in lower lasing level j.

The dipole matrix element is given by [64]

$$z_{ij} = \frac{\hbar}{2(E_j - E_i)} \left\langle \psi_i \middle| p_z \frac{1}{m^*(E_i, z)} + \frac{1}{m^*(E_j, z)} p_z \middle| \psi_j \right\rangle, \tag{3.3}$$

where the energy dependent effective mass is given by

$$m^*(E) = m^*(E = 0) \left(1 + \frac{E - V}{E_g} \right). \tag{3.4}$$

In Eq. (3.4), E is the electron energy and V is the energy of the conduction band edge.

The gain linewidth of a QCL with the lasing transition from subband i to subband j is given by

$$2\gamma_{ij} = \hbar \left(\frac{1}{\tau_{i \to j}} + \frac{1}{\tau_{i \to i}} + \frac{1}{\tau_{j \to j}} \right), \tag{3.5}$$

where $\tau_{i\to j}$ is the lifetime of electrons due to inter-subband scattering between subbands i and j and $\tau_{i\to i}$ is the intra-subband scattering lifetime in subband i. Among the different inter-subband scattering mechanisms in QCLs, electron-LO phonon scattering rate is greater than that of other mechanisms by at least an order of magnitude [65]. However, electron scattering rate due to interface roughness within the subbands in QCLs becomes significant [66]. Therefore, in this work, we calculate the inter-subband lifetimes considering electron scattering due to LO phonons only and intra-subband lifetimes considering electron scattering due to interface roughness and LO phonons. This modeling approach for gain linewidth agrees well with experiments [67].

We calculate the carrier densities in the subbands using the rate equation approach that has been discussed in [68]. The rate equations that we solve are given by [68]

$$\frac{dn_j}{dt} = \sum_{i=1,i\neq j}^{N} \frac{n_i}{\tau_{ij}} - n_j \sum_{i=1,i\neq j}^{N} \frac{1}{\tau_{ji}}, \tag{3.6}$$

where n_i is the carrier density in level i and τ_{ij} is the scattering lifetime from subband i to subband j. As we have mentioned before, electron-LO phonon scattering is much more dominant among the scattering mechanisms of inter-subband transitions. Therefore, we have calculated the scattering lifetimes considering only the electron-LO phonon scattering. Equation (3.6) is formulated assuming periodicity of the quantum-cascade structure, i.e., the electrons extracted from an active region are injected into the injector region of the next period. In this approach, we do not solve the rate equations in k-space. However, we calculate the scattering rates assuming that the carriers are distributed at high in-phase k-values,

which depends on the temperature and carrier density of the subband. Then the scattering rates are calculated taking the average assuming Fermi distribution of the carriers. In this approach, initially, we distribute the carriers equally among the energy levels in the injector region. The carrier densities are redistributed in the injector and active region energy levels as the rate equations are solved with respect to time. Finally, we get steady-state carrier densities in a time scale greater than the scattering lifetimes of the states.

Γ is the confinement factor given by [69]

$$\Gamma = 0.3 N_w \frac{L}{L_o}, \tag{3.7}$$

where N_w is the number of quantum wells, L is the thickness of single quantum well and L_o is an arbitrary parameter taken to be 1000Å.

The peak emission gain has been collected from the gain spectrum which is plotted using the Lorentzian lineshape given by [64]

$$L(E_{ij}) = \left[1 + \left(\frac{E_{ij} - E_o}{2\gamma_{ij}}\right)^2\right]^{-1}, \tag{3.8}$$

where E_{ij} is the energy difference between sub-bands i and j and E_o is the photon energy. Lorentzian lineshape given by Eq. (3.8) determines the peak of the gain spectrum.

The gain spectrum of the QCL can be plotted using the following equation,

$$G = G_m L(E_{ij}), \tag{3.9}$$

where G_m is the peak modal gain given by Eq. (3.1) and $L(E_{ij})$ is the Lorentzian lineshape given by Eq. (3.8).

3.2.2 Mode

Modes of QCLs depend on the cavity length and effective refractive index of the cavity. The two mirrors of the laser form a resonant cavity and standing wave patterns are set up between the mirrors in exactly the same way that standing waves develop on a string or within an organ pipe. Thus, the resonant frequencies of the QCL is given by [7]

$$f = m\frac{c}{2nL}, \tag{3.10}$$

where m is an integer, c is the speed of light and L is the cavity length of QCL. Each value of m satisfying Eq. (3.10) defines an axial or longitudinal mode of the cavity. While all the integer m's give possible axial cavity modes, only those which lie within the gain curve above the loss line can be sustained in the cavity.

3.2.3 Gain Spectrum

For the QCL structure described in Sec. 2.3, the gain spectrum has been plotted with the axial modes in Fig. 3.1. In this figure, only those axial modes have been shown which are above both the loss line and the FWHM. The cavity length has been considered to be 1 mm and the refractive index is 3.27. Thus in this

condition, only the modes shown can exist as radiation in the cavity, that is, for propagation along the cavity axis.

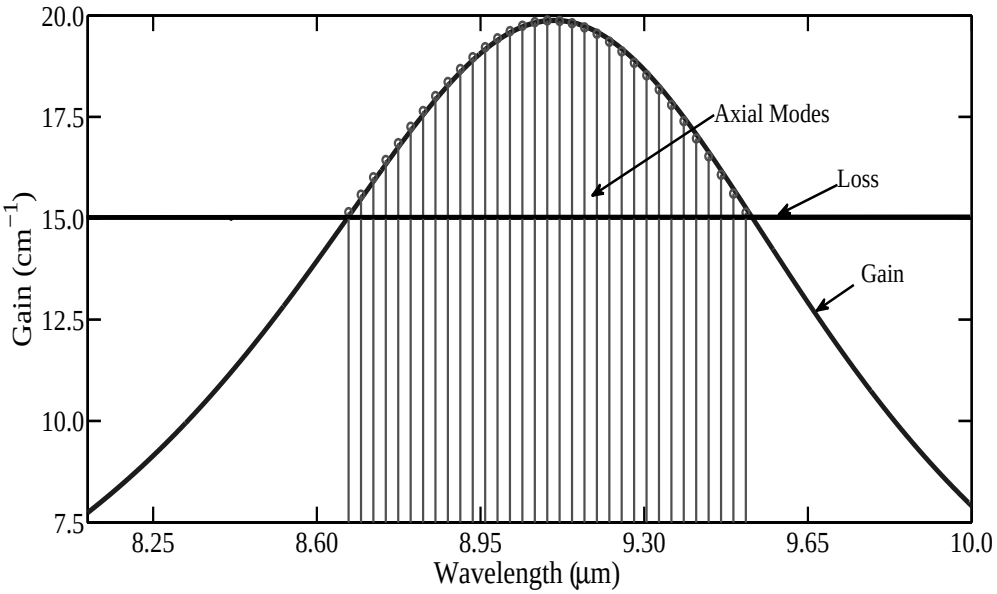

Figure 3.1: Gain spectrum of the QCL structure of Sec. 2.3 with loss line and axial modes.

From the gain spectrum of Fig. 3.1, we can see that peak gain occurs at a wavelength of $\sim$ 9 μm. This matches quite perfectly with the Bragg wavelength ($\lambda_B = 2n\Lambda/m$) of 8.988 μm that has been calculated with $m = 1$ (first order grating), 3.21 guide material refractive index (n) and 1.4 μm grating period (Λ). Also, the wavelengths of the allowed modes span a wavelength range from about 8.65 μm to 9.35 μm.

For a multi-mode or Fabry-Perot QCL, the output of the laser will be the modes which have gain above the losses of the laser cavity. Amongst these modes we

consider the mode nearest to peak to be the fundamental emission mode. For single mode DFB-QCL, a resonator is attached to the laser cavity by creating a grating into the top cladding layer so that light of only one single frequency or mode is emitted. The laser emits light as long as the gain of that mode is above the losses of the laser. It produces a finer range of wavelengths than a Fabry-Perot cavity as it has a a Bragg reflector (BR) built on top of the waveguide to allow emission of desired wavelength only. This forces single mode operation of the laser at all operating conditions as will be shown in Sec. 3.4.1 for rectangular gratings and in Sec. 3.4.2 for trapezoidal gratings.

3.3 FDTD Simulations of DFB-QCLs

We have performed our analysis using the QCL structure of Sec. 2.3 and the rectangular and trapezoidal waveguide structures of Sec. 2.4. In order to find out the output emission characteristics of DFB-QCLs, we have used the finite-difference time-domain (FDTD) method for calculating the electric field intensity of output emission of the QCL and associated optical power with varying wavelength.

In a DFB laser, radiation is fed from the active into the corrugated layer along the whole cavity length so that the corrugating medium can be thought of as possessing an optical gain. Traveling waves are reflected partially and periodically as they propagate. The left and right traveling waves can only coherently couple to set up a mode if their frequency is related to the corrugation periodicity (Λ).

To model this behavior, we have simulated the waveguide for output power and

electric field intensity using Lumerical FDTD Solutions, the details of which are given in Appendix B. We have used a mode source that is placed on one side of the waveguide. It has been designed to emit electromagnetic radiation that has the peak emission wavelength equal to the Bragg wavelength (λ_B), and a FWHM calculated from the gain spectrum of the QCL. This multi-mode emission is incident on one side of the DFB-QCL waveguide and travel across the cavity length.

We have used mode source in our simulation. The mode source is used to inject a guided mode into the simulation region. In two-dimensional simulations the modes are computed across a line. From the calculated gain spectrum of the QCL, we have selected a wavelength range with modes having higher gain than both the FWHM and the assumed loss for the structure. From the gain spectrum of Fig. 3.1, we see that the wavelengths of the allowed modes span a wavelength range from about 8.65 μm to 9.35 μm. This range has been used in the mode source in our simulation. The output spectrum of the source is shown in Fig. 3.2.

Boundary conditions are very important in electromagnetics and simulation techniques. FDTD supports a range of boundary conditions, such as perfectly matched layer (PML), periodic, and Bloch. We have used PML for our simulation purpose. PML boundaries absorb electromagnetic energy incident upon them and allow radiation to propagate out of the computational area without interfering with the fields inside [70]. Furthermore, PML boundaries perform best when the surrounding structures extend completely through the boundary condition region.

We have used 1 mm cavity so that considering rectangular grating with 1.4 μm

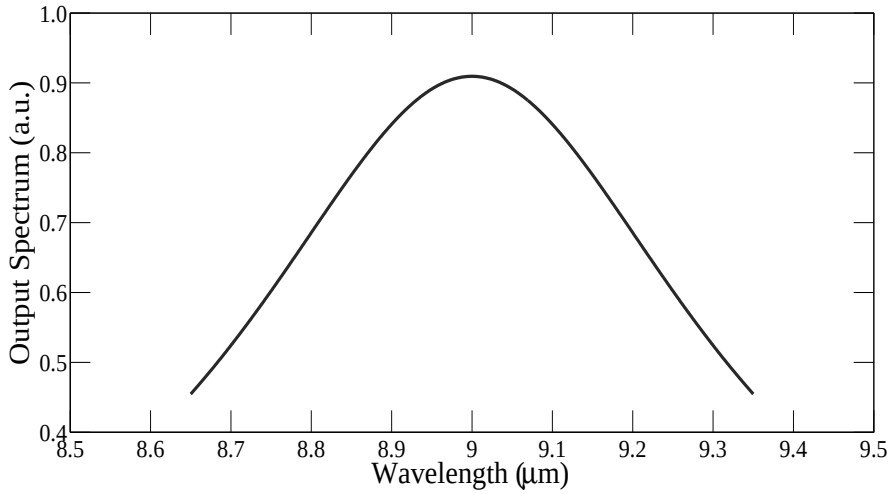

Figure 3.2: Output spectrum of the source used in FDTD solutions.

period and 500 nm depth, the value of κL is approximately 3. This value is slightly higher than typically calculated from experimental data (close to 1-1.5) [30, 71], which suggests that the device is slightly overcoupled. This overcoupling is helpful to secure single-mode operation at high operating currents [12]. The waves propagate through the waveguide that acts as a wavelength dependent mirror. Strong reflection occurs for a particular wavelength when $2\Lambda = m\lambda_B/n$, where Λ is the grating period, λ_B is the Bragg wavelength, n is the effective refractive index of the medium and m is an integer. On the opposite side of the structure, a monitor is placed to capture the frequency-domain field profile that calculates the output optical power with varying wavelength. The schematic of the model is shown in Fig. 3.3.

We have considered 500 ps to be the total simulation time for the DFB-QCL. This gives sufficient time for the electromagnetic radiation to propagate through

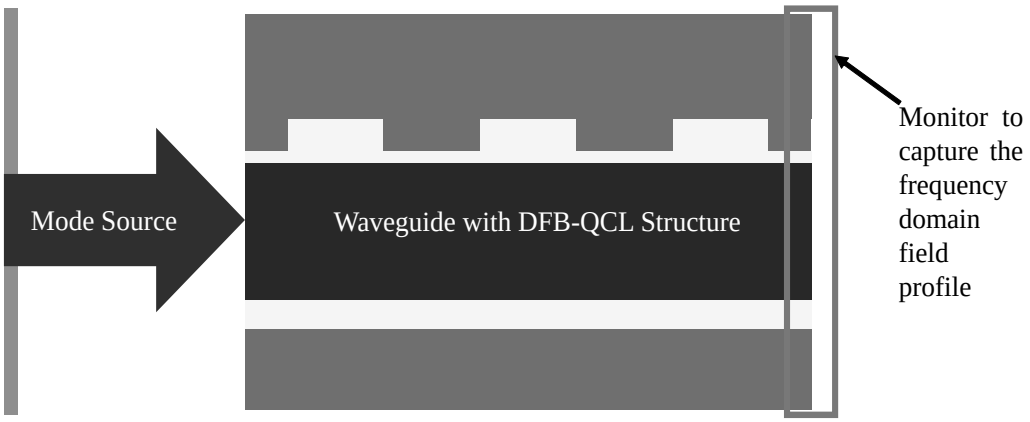

Figure 3.3: Schematic illustration of the DFB-QCL structure used in Lumerical FDTD Solutions to analyze its output characteristics.

the structure and reflect at each end several times so that a stable single mode is achieved on the output. For example, for a refractive index of 3.27 and a 1 mm cavity, the wave travels back and forth for a total of ~46 times.

3.4 Results

We have performed the FDTD solutions to find out the output power of the devices of Sec. 2.4 by the process described in Sec. 3.3. We have considered both rectangular and trapezoidal gratings with three corrugation periods of 1.3 μm, 1.4 μm, and 1.5 μm and five grating depths of 100 nm, 300 nm, 500 nm, 800 nm, and 1000 nm for each period. The results of our analysis are given in this section.

3.4.1 Rectangular Grating

From Chap. 2, we have found that the value of the coupling coefficient (κ) is highest for a tooth angle of 90°, i. e., the grating is of rectangular shape. Here we have

calculated the output optical power of a DFB-QCL using FDTD technique with light injected through one of the facets and collected from the other facet after the light has propagated back and forth several times. We have calculated the output optical power for three different cases of 1.3 μm, 1.4 μm, and 1.5 μm grating period.

1.3 μm Grating Period

For 1.3 μm grating period, the Bragg wavelength is ~8.5 μm. As we consider only those modes above both the loss line and FWHM of the gain spectrum, we choose the wavelength range from 8.15 μm to 8.85 μm. Since we found in Sec. 2.6.2 that the value of κ reaches its peak with a grating depth of 500 nm, we have first plotted the output power with a grating depth of 500 nm in Fig. 3.4.

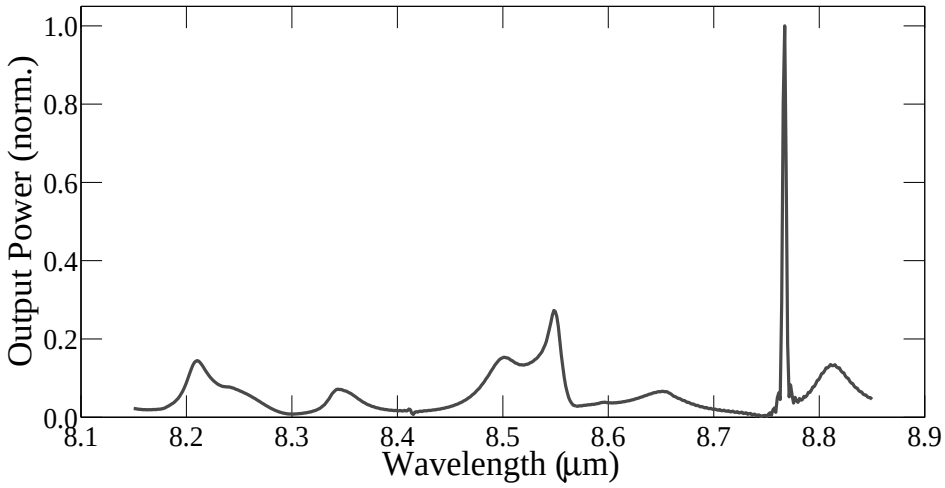

Figure 3.4: Output power of the DFB-QCL of Fig. 2.4 with 1.3 μm rectangular grating period and 500 nm grating depth.

The output powers for different wavelengths have been normalized with respect to the peak output power for a wavelength of ~8.76 μm. This mode has the highest optical power associated with it and is more likely to lase from the cavity. To compare this with other devices with different grating depths, we perform FDTD simulations and obtain the results given in Fig. 3.5.

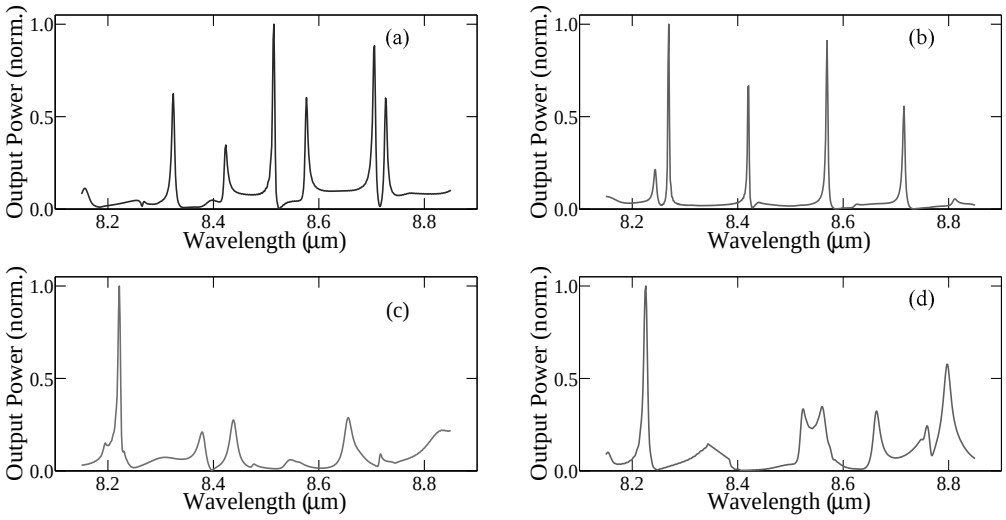

Figure 3.5: Output power of the DFB-QCL of Fig. 2.4 with 1.3 μm rectangular grating period for (a) 100 nm, (b) 300 nm, (c) 800 nm, and (d) 1000 nm grating depth.

From Sec. 2.6.2, we know that for our chosen waveguide structure the value of κ increases with increasing grating depth upto 500 nm, and then remains almost constant. Therefore, we get a single peak for a DFB-QCL with a grating depth of 500 nm and multi-peaks for DFB-QCLs with grating depths of 100 nm and 300 nm. For DFB-QCLs with grating depths of 800 nm and 1000 nm, although the results show a distinct mode at ~8.22 μm, the side-mode suppression ratio (SMRR), which is the ratio of power between peak longitudinal mode with the next higher

order mode, is lower than that DFB-QCL with a 500 nm grating depth.

1.4 μm Grating Period

For 1.4 μm grating period, the Bragg wavelength is ~9 μm. As we consider only those modes above both the loss line and FWHM of the gain spectrum, we choose the wavelength range from 8.65 μm to 9.35 μm. Since we found in Sec. 2.6.2 that the value of κ reaches its peak with a grating depth of 500 nm, we have first plotted the output power with a grating depth of 500 nm in Fig. 3.6.

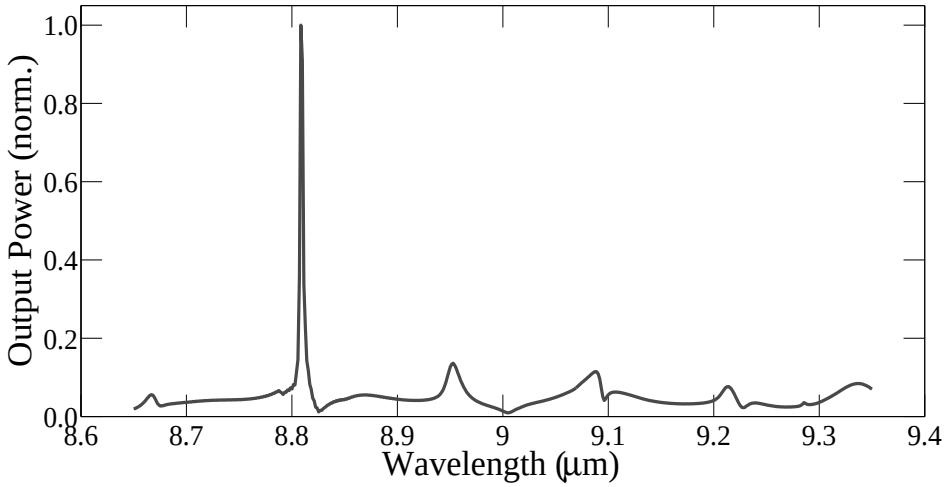

Figure 3.6: Output power of the DFB-QCL of Fig. 2.4 with 1.4 μm rectangular grating period and 500 nm grating depth.

As is shown in Fig. 3.6, from a range of wavelengths emitted from the mode source, the DFB grating allows only one mode with a wavelength of 8.81 μm to oscillate within the laser cavity. Also, if we compare the result with that obtained from a DFB-QCL with a grating period of 1.3 μm, we note that the SMSR is also

better in this case. The greater value of SMSR can be attributed to the greater value of κ in the case of 1.4 μm grating period than that in the case of 1.3 μm grating period. We next compare this with other devices with different grating depth, but same grating period in Fig. 3.7.

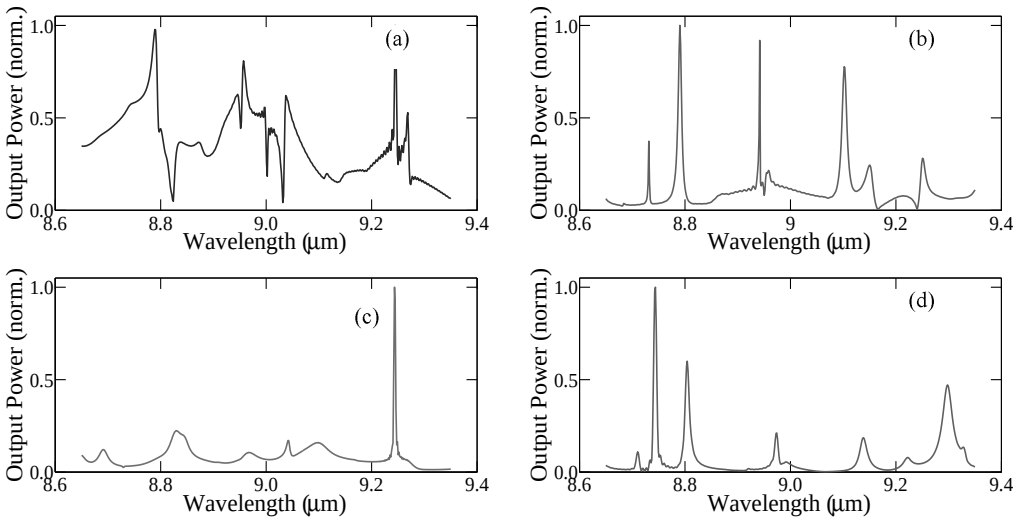

Figure 3.7: Output power of the DFB-QCL of Fig. 2.4 with 1.4 μm rectangular grating period for (a) 100 nm, (b) 300 nm, (c) 800 nm, and (d) 1000 nm grating depth.

The performance of the 100 nm depth DFB is quite unsatisfactory. The value of κ for this device is as low as 10.35 cm^{-1} and there is very little coupling between the forward and backward moving waves, resulting in poor single-mode selection by the device. The DFB-QCL with a grating depth of 300 nm has also multi-peaked output power spectrum with dominating modes at about 8.79, 8.95, and 9.1 μm. By contrast, the output spectra of the DFB-QCL with a grating depth of 800 nm is single-peaked at 9.24 μm, while that of the DFB-QCL with a grating depth of 1000 nm has a dominant side mode. The values of κ are almost equal in the cases

when the grating depth is 500 nm and 800 nm. Therefore, we note single-mode operation to occur with 500 nm and 800 nm grating. We note that the SMSR is greater in the case of 1.4 μm grating period than that of 1.3 μm grating period.

1.5 μm Grating Period

For 1.5 μm grating period, the Bragg wavelength is ~9.6 μm. As we consider only those modes above both the loss line and FWHM of the gain spectrum, we choose the wavelength range from 9.25 μm to 9.95 μm. Since we found in Sec. 2.6.2 that the value of κ reaches its peak with a grating depth of 500 nm, again we have first plotted the output power with a grating depth of 500 nm in Fig. 3.8.

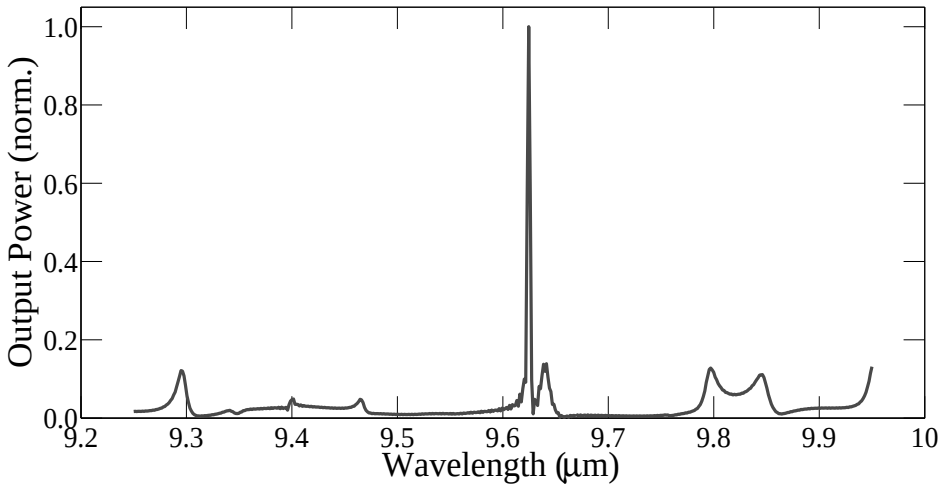

Figure 3.8: Output power of the DFB-QCL of Fig. 2.4 with 1.5 μm rectangular grating period and 500 nm grating depth.

We note that the output power is concentrated at a wavelength of ~9.62 μm. The linewidth of the mode is also very small, on the order of nm, as is expected from

a DFB laser [63]. The value of κ reaches its peak for this structure at 37.47 cm^{-1}. This results in the lower value of the linewidth compared with those DFB-QCLs with grating periods of 1.3 μm and 1.4 μm Figs. 3.4 and 3.6 respectively, which means that this device has higher modal purity. We next plot the output power for four other grating depths in Fig. 3.9.

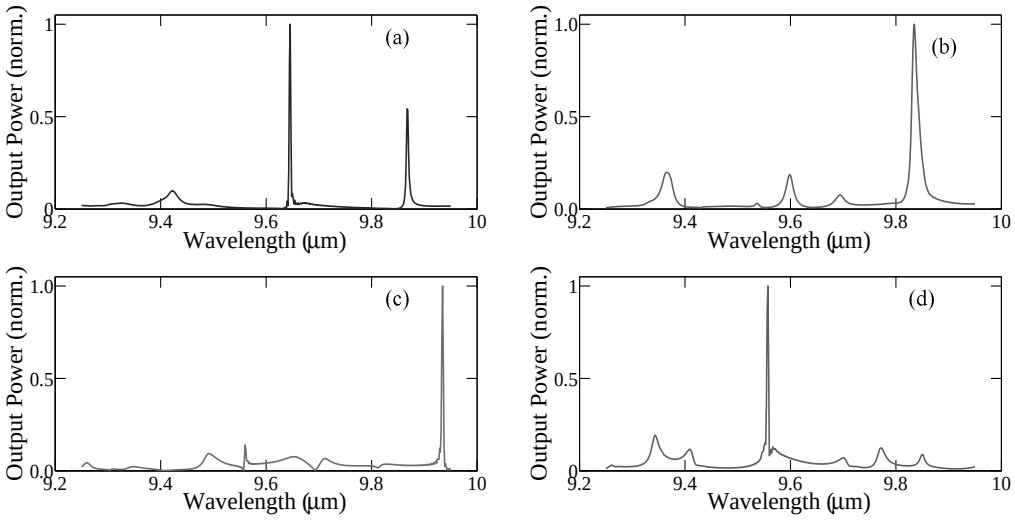

Figure 3.9: Output power of the DFB-QCL of Fig. 2.4 with 1.5 μm rectangular grating period for (a) 100 nm, (b) 300 nm, (c) 800 nm, and (d) 1000 nm grating depth.

We see that the high value of κ for 1.5 μm period devices (shown in Fig. 2.9) makes them oscillate at a single-mode for almost all grating depths. In this case, the performance of DFB-QCLs with grating period of 1.5 μm and grating depths depths of 100 nm and 300 nm in obtaining a single-mode emission is better than those DFB-QCLs with same grating depths but grating periods of 1.3 μm and 1.4 μm. The DFB-QCL with grating depth of 100 nm has two peaks at ~9.65 and ~9.86 μm, while the DFB-QCL with grating depth of 300 nm is single-peaked

at ~9.84 μm. Both DFB-QCLs with grating depths of 800 nm and 1000 nm are single-peaked at ~9.93 and ~9.56 μm respectively. Also, for each grating depth, the SMSR is also much better than the previous shorter period devices.

Comparison between Three Grating Periods

We next compare the relative output power for all the three grating periods. If we plot the output power for 500 nm grating depth devices of the 1.3, 1.4 and 1.5 μm period, we can compare their relative output power. The plot is shown in Fig. 3.10.

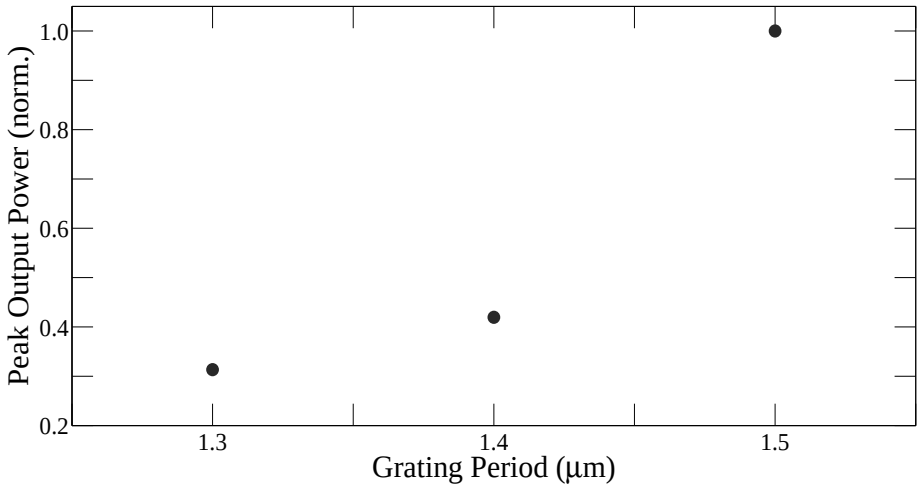

Figure 3.10: Comparison of Output power of the DFB-QCL of Fig. 2.4 with three different periods and 500 nm grating depth.

The output power increases with increasing grating period. It increases significantly if we increase the period to 1.5 μm. This means that when the output power from a laser is a big concern, the longer period DFB-QCLs should be used.

3.4.2 Trapezoidal Grating

It is important to analyze DFB-QCLs with trapezoidal shaped gratings since fabrication processes are more likely to build trapezoidal gratings than rectangular ones [45]. Thus, we have calculated the optical power for the trapezoidal grating devices for three different cases of 1.3 μm, 1.4 μm, and 1.5 μm grating period.

1.3 μm Grating Period

For 1.3 μm grating period, the Bragg wavelength is ~8.5 μm. As we consider only those modes above both the loss line and FWHM of the gain spectrum, we choose the wavelength range from 8.15 μm to 8.85 μm.

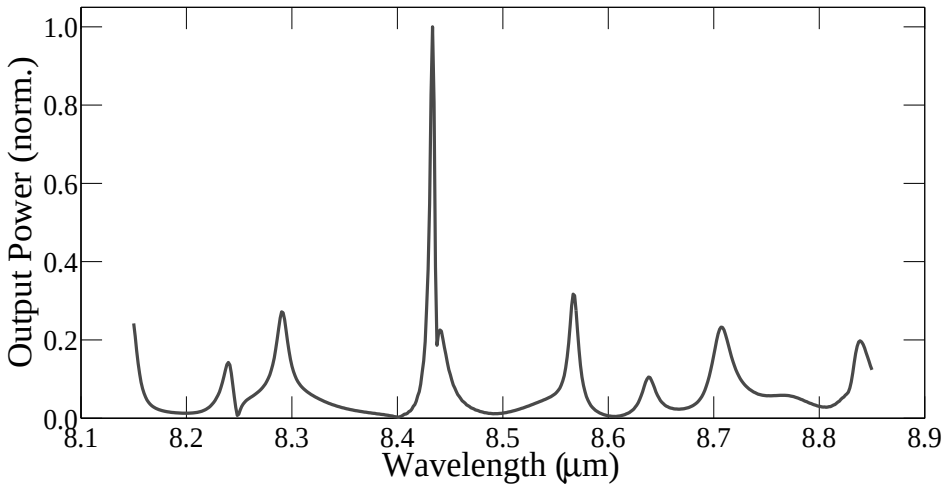

Figure 3.11: Output power of the DFB-QCL of Fig. 2.11 with 1.3 μm trapezoidal grating period and 500 nm grating depth.

We have first plotted the output power with a grating depth of 500 nm in Fig. 3.11.

Although there is a distinct peak at ~8.44 μm, the SMSR for this device is quite poor. We compare this with four other grating depths in Fig. 3.12.

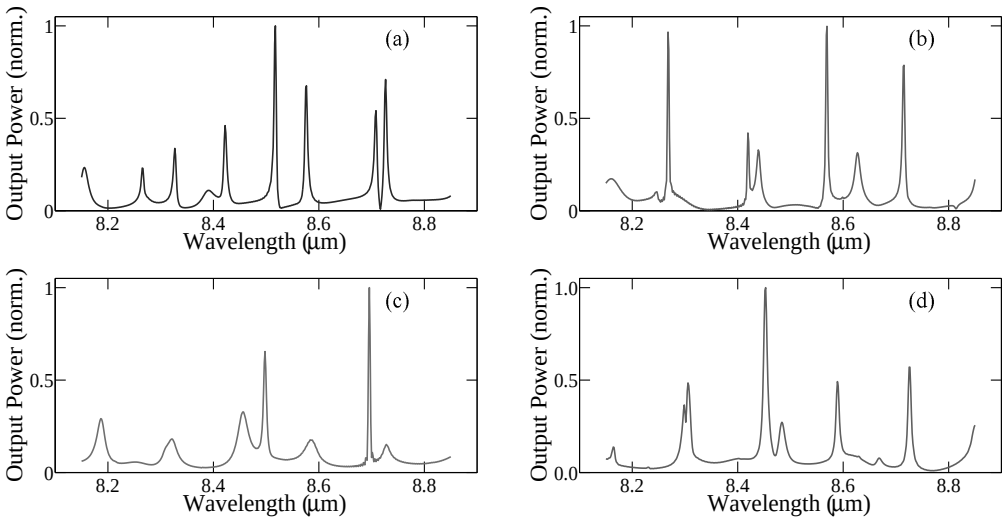

Figure 3.12: Output power of the DFB-QCL of Fig. 2.11 with 1.3 μm trapezoidal grating period for (a) 100 nm, (b) 300 nm, (c) 800 nm, and (d) 1000 nm grating depth.

We can see from Fig. 3.12 that almost all DFB-QCLs with 1.3 μm period of trapezoidal grating have poor performance in terms of single-mode selection. The DFB-QCL with grating depth of 100 nm has several distinct modes with comparable intensity, while the DFB-QCL with grating depth of 300 nm has three distinct peaks. Although the DFB-QCLs with grating depths of 800 nm and 1000 nm have one distinct peak, both of them have very low SMSR. This is due to the lower grazing angle of the trapezoidal gratings ($< 90°$). From Sec. 2.6.3, we know that the lower the grazing angle, the lower the value of the coupling coefficient. Therefore, in case of DFB-QCLs with 1.3 μm period of trapezoidal grating, the value of κ is lower than those of rectangular gratings (Fig. 2.9), resulting in poor

single-mode selection of the devices.

1.4 μm Grating Period

For 1.4 μm grating period, the Bragg wavelength is ~9 μm. As we consider only those modes above both the loss line and FWHM of the gain spectrum, we choose the wavelength range from 8.65 μm to 9.35 μm. Since we found in Sec. 2.6.2 that the value of κ reaches its peak with a grating depth of 500 nm, we have first plotted the output power with a grating depth of 500 nm in Fig. 3.13.

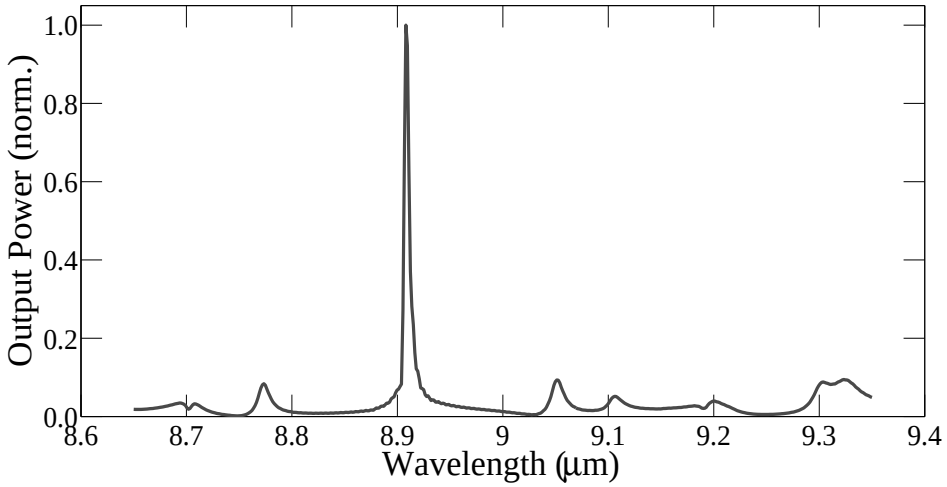

Figure 3.13: Output power of the DFB-QCL of Fig. 2.11 with 1.4 μm trapezoidal grating period and 500 nm grating depth.

As is shown in Fig. 3.6, in terms of single-mode selection, this DFB-QCL with grating period of 1.4 μm has better performance than the DFB-QCL with grating period of 1.3 μm. From a range of wavelengths emitted from the mode source, the DFB grating allows only one mode with a wavelength of ~8.91 μm to oscillate

within the laser cavity. Also, if we compare the result with that of 1.3 μm period (shown in Fig. 3.11), we see that the SMSR is also better in this case. This can be attributed to higher value of κ for DFB-QCLs with 1.4 μm period than those DFB-QCLs with 1.3 μm period. We next compare this with other devices with different grating depth, but same grating period in Fig. 3.14.

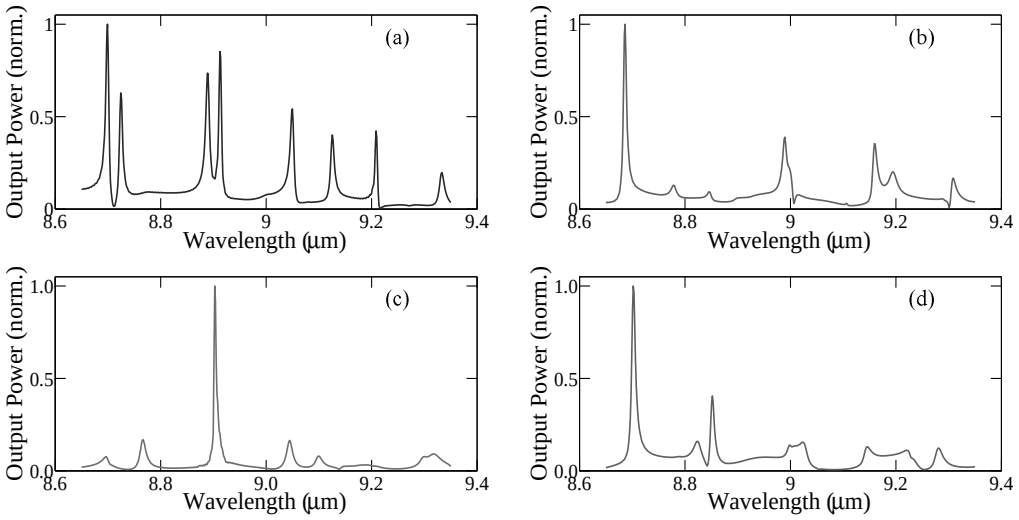

Figure 3.14: Output power of the DFB-QCL of Fig. 2.11 with 1.4 μm trapezoidal grating period for (a) 100 nm, (b) 300 nm, (c) 800 nm, and (d) 1000 nm grating depth.

We see that the DFB-QCL with 1.4 μm grating period shows better performance than that with 1.3 μm period. The DFB-QCLs with grating depths of 100 nm and 300 nm devices are still multi-peaked but with better SMSR. Both DFB-QCLs with grating depths of 800 nm and 1000 nm are single-peaked at ~8.91 μm and ~8.71 μm respectively. The performances of the DFB-QCLs with grating depths of 500 nm and 800 nm device are comparable in terms of their single-mode selection. This can be attributed to their close value of the coupling coefficient.

1.5 μm Grating Period

For 1.5 μm grating period, the Bragg wavelength is ~9.6 μm. As we consider only those modes above both the loss line and FWHM of the gain spectrum, we choose the wavelength range from 9.25 μm to 9.95 μm. Since we found in Sec. 2.6.2 that the value of κ reaches its peak with a grating depth of 500 nm, again we have first plotted the output power with a grating depth of 500 nm in Fig. 3.15.

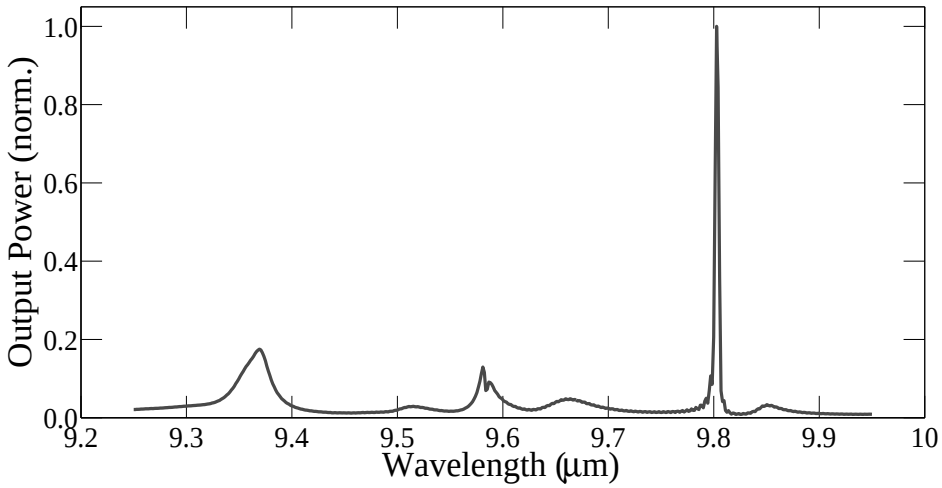

Figure 3.15: Output power of the DFB-QCL of Fig. 2.11 with 1.5 μm trapezoidal grating period and 500 nm grating depth.

We note that the output power is concentrated at a wavelength of ~9.8 μm. Like that DFB-QCL with rectangular grating and 1.5 μm grating period, the linewidth of the mode is also very small, on the order of nm, but slightly higher than that of the rectangular grating. The value of κ is highest for this structure, but still lower than the DFB-QCL with rectangular grating due to its lower tooth angle.

This results in the higher value of the linewidth compared with that for rectangular grating in Fig. 3.8. We next plot the output power for four other grating depths in Fig. 3.16.

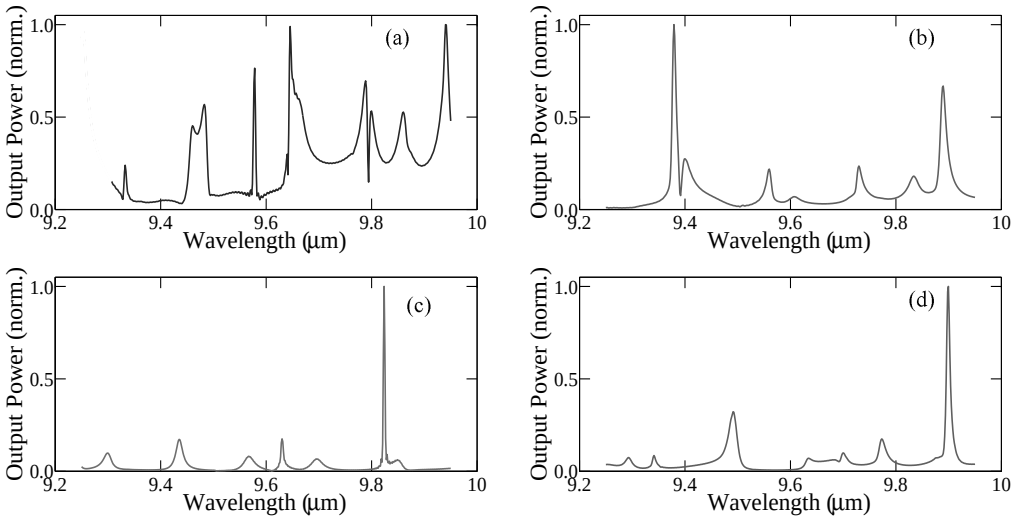

Figure 3.16: Output power of the DFB-QCL of Fig. 2.11 with 1.5 μm trapezoidal grating period for (a) 100 nm, (b) 300 nm, (c) 800 nm, and (d) 1000 nm grating depth.

We see that except for the DFB-QCL with grating depth of 100 nm, all the other structures have distinct peaks due to the higher values of κ as shown in Fig. 2.9. The DFB-QCL with grating depth of 100 nm has many peaks of comparable intensity. The DFB-QCL with grating depth of 300 nm device is single-peaked at ~9.38 μm, but has a lower SMSR. Both DFB-QCLs with grating depths of 800 nm and 1000 nm devices are single-peaked at ~9.82 and ~9.9 μm respectively. Also, for each grating depth, the SMSR is also much better than the previous shorter period devices with trapezoidal grating.

Comparison between Three Grating Periods

We next compare the relative output power for all the three grating periods with trapezoidal grating shape. If we plot the output power for 500 nm grating depth devices of the 1.3, 1.4 and 1.5 μm period, we can compare their relative output power. The plot is shown in Fig. 3.17.

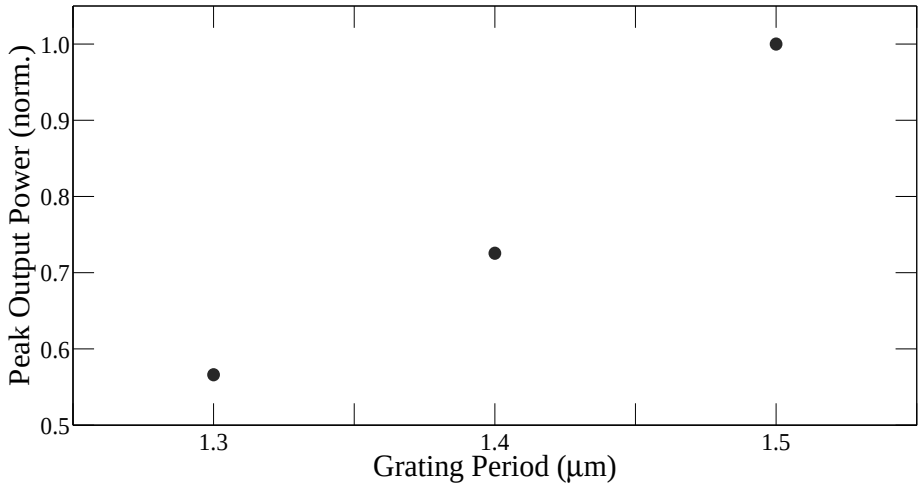

Figure 3.17: Comparison of Output power of the DFB-QCL of Fig. 2.11 with three different periods and 500 nm grating depth.

As expected, we see from Fig. 3.17 that the output power increases with increasing grating period. The value of output power increases slightly from 1.3 μm to 1.5 μm grating period. It then increases more if we increase the period to 1.5 μm, but the amount of increase is not as significant as it was for the rectangular grating.

3.4.3 Comparison between Rectangular and Trapezoidal Grating

We have seen so far that the performance of the rectangular shaped grating DFB-QCLs is better than those with trapezoidal shaped grating. We plot the output optical power of the 1.5 μm period and 500 nm depth devices with both rectangular and triangular shape on the same plot in Fig. 3.18.

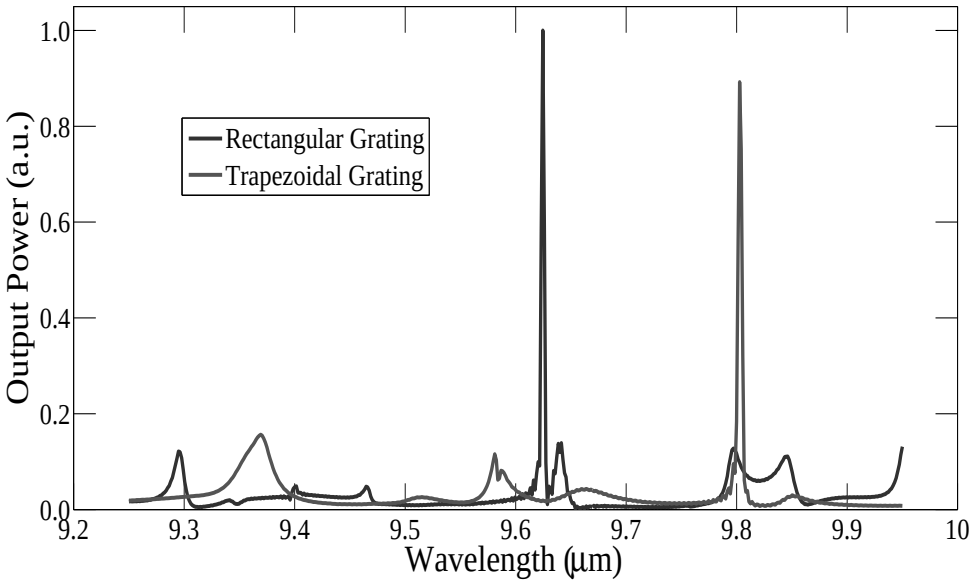

Figure 3.18: Comparison of Output power of the DFB-QCL of Rectangular and Trapezoidal grating shape.

We note that both devices have single peak, but the rectangular one has slightly higher intensity compared to the trapezoidal one. This is due to the higher value of κ for rectangular grating than for trapezoidal grating. In Table 3.1 we give a brief summary of the single-mode selection performance of all the devices that we

have analyzed.

Table 3.1: Summary of Mode-Selection Performances of the DFB-QCLs analyzed in Chap. 3.

Shape	Period (μm)	Mode Profile				
		100 nm	300nm	500 nm	800 nm	1000 nm
Rectangular	1.3	Multiple	Multiple	Single	Single	Single
	1.4	Multiple	Multiple	Single	Single	Multiple
	1.5	Multiple	Single	Single	Single	Single
Trapezoidal	1.3	Multiple	Multiple	Single	Single	Multiple
	1.4	Multiple	Single	Single	Single	Single
	1.5	Multiple	Single	Single	Single	Single

Next we see the effect of the DFB grating on the gain spectrum of the QCL. From Fig. 3.1, we know that there are many modes that have gain higher than the loss or FWHM of the QCL. In a Fabry-Perot QCL, which is multi-mode device, many of these modes will be available in the laser output. But using a DFB-QCL can select only one output mode. To see the effect of DFB-QCL on the gain spectrum, we plot the output optical power for the 1.5 μm period rectangular and trapezoidal grating on the gain spectrum of the QCL in Fig. 3.19.

We note from Fig. 3.19 that use of DFB grating on the top cladding of the waveguide structure has made it possible to select a single mode from a multi-mode gain spectrum of the QCL.

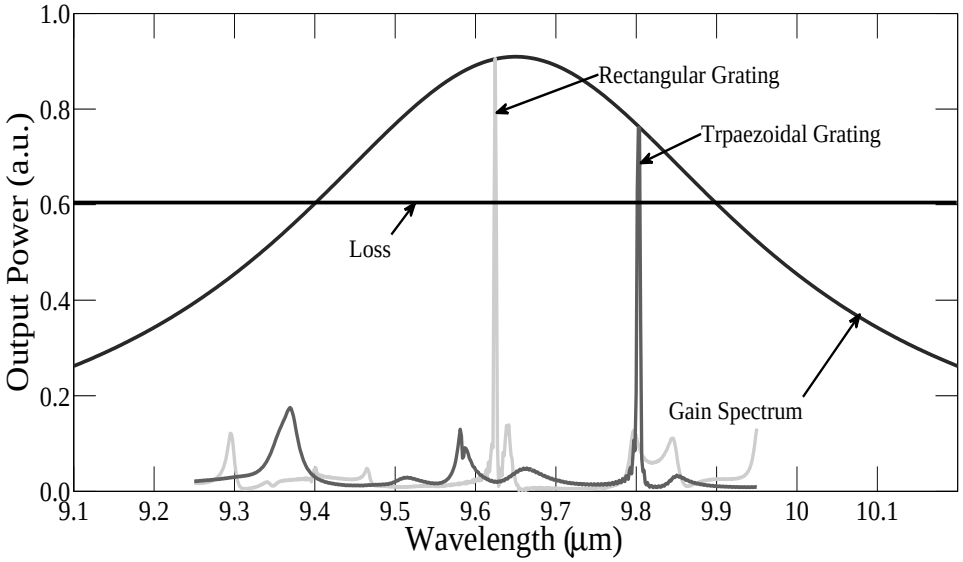

Figure 3.19: Effect of DFB grating on the gain spectrum of QCL.

3.4.4 Effect of Second Order Grating

We have seen in Sec. 2.6.4 that the coupling coefficient is smaller for a second order grating than that for a first order grating. This implies that the second order grating will show a poorer performance in terms of single mode selection than a first order grating does. This is coherent with the works of [72]. We can explain this result by considering that for a specific wavelength and for a resonator length L, in order to maintain the Bragg wavelength ($\lambda_B = 2n\Lambda/m$) for the second-order corrugation ($m = 2$), the second-order grating period must be twice of that of the first-order value. Hence the number of the grating period decreases in the resonator's length. As a result, the efficiency of the feedback process by the grating decreases and hence the coupling between different waves decreases. Therefore, the single-mode selection by the second order diffraction grating will not be as efficient as the first order grating.

3.4.5 Selection of a Traget Wavelength

We have varied the grating shape, depth, and period of the corrugation in the top cladding layer of the waveguide structure and observed their effects on the coupling coefficient as well as the output optical power of DFB-QCLs. We have found that DFB-QCLs with 1.5 μm grating period of rectangular shape are best at selecting a single mode from a multi-mode source. We take the peak emission wavelengths for DFB-QCL with a rectangular grating period of 1.5 μm and various grating depths and plot the results in Fig. 3.20 where the peak emission wavelengths have been plotted against grating depths (red circles).

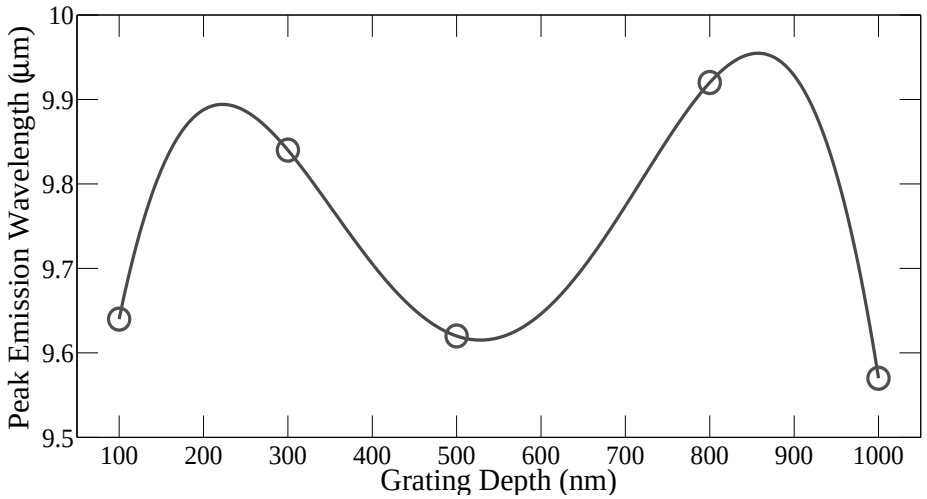

Figure 3.20: Calculated peak emission wavelengths for a DFB-QCL with 1.5 μm rectangular grating (red circles) and the polynomial function that fits the data-set (green curve).

In Fig. 3.20, we also show a fourth degree polynomial function that has been calculated using the Curve Fitting Tool of MATLAB (green curve). This curve predicts a peak emission wavelength for a specific grating depth. To check the

validity of the curve, we plot the output optical power for a grating depth of 700 nm. The result is shown in Fig. 3.21.

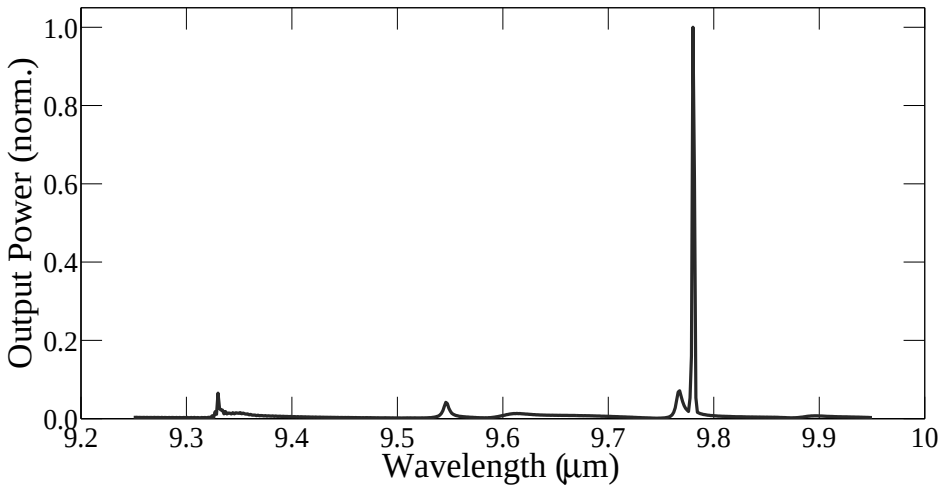

Figure 3.21: Output power of the DFB-QCL of Fig. 2.4 with 1.5 μm rectangular grating period and 700 nm grating depth.

We see that the DFB-QCL with a grating depth of 700 nm shows a distinct peak at ~9.78 μm. From our 4th degree polynomial function in Fig. 3.20, we note that the curve predicts a peak emission wavelength at ~9.76 μm, which is very close to the value found from the output spectrum of Fig. 3.21. Therefore, we have designed a model to select a specific peak emission wavelength that is dependent on the grating depth of the DFB-QCL, provided we fit the polynomial functions for the grating period for which the coupling coefficient is highest.

3.5 Summary

The DFB-QCL is used to ensure a single mode of radiation in the laser cavity. In Chap. 3, we have analyzed the output characteristics of various DFB-QCLs with different grating shapes, periods, and depths. The key points of this chapter are summarized here.

- We have presented a full-vectorial FDTD model for analysis of wave propagation inside the cavity.
- The rectangular shaped gratings with higher coupling coefficients are better at selecting a single-mode for oscillation than the trapezoidal shaped gratings.
- Analysis of trapezoidal shaped gratings is still important since practical fabricated devices are more likely to have a trapezoidal grating, rather than rectangular grating.
- As we increase the grating depth, the single-mode selection performance of the devices gets better upto 500 nm (for our structure). After that it slightly worsens. This behavior is supported the values of the coupling coefficient for different grating depths.
- There is an optimum grating depth for each DFB-QCL waveguide, for which the DFB selects a mode to lase with much higher intensity than any other allowed modes inside the laser cavity.
- The ability to select a single mode gets better with increasing grating period of the DFB-QCL. For our chosen structure, the performance is best for a

rectangular grating with 1.5 μ grating period.

- We have shown the effect of DFB grating in single-mode selection for oscillation from a multimode QCL gain medium.
- A design rule based on the obtained results has been proposed for selecting a specific wavelength for lasing.

Chapter 4

Conclusion

QCL is a semiconductor laser that emits highly coherent radiation in the mid- to long-wave infrared region of the spectrum, where almost any molecule has a strong absorption band. They have many advantages over other types of semiconductor lasers such as Lead Salt Diode lasers or Diode lasers. Some of the advantages include precise tuning from one wavelength to another, higher optical power, continuous wave operation and the ability to produce light in the terahertz range of the spectrum, small and light to make portable systems.

A DFB-QCL has a diffraction grating grown on the cladding of the active region. This grating provides narrow band optical feedback, distributed along the length of the waveguide, eliminating the need for discrete mirrors to form an optical cavity. DFBs allow for semi-stable fixed wavelength sources. A Fabry-Perot (FP) QCL uses the cleaved facet ends of the cavity to form two reflective surfaces. Since the wavelengths are reflected equally in a FP QCL, all wavelengths in the gain profile of the laser are available for lasing. DFB-QCL also has multiple ax-

ial resonator modes, but there is typically one mode which is favored in terms of losses. Therefore, single-frequency operation is often easily achieved with DFB-QCLs.

To understand the working mechanism of a DFB-QCL, the coupling coefficient is one of the most important parameters to be considered. In this thesis, we have developed a model to calculate the coupling-coefficient of DFB-QCLs. We have also observed the behavior of the coupling coefficient with changing parameters like temperature, grating depth, grating period, tooth angle, duty cycle, and grating shape. We found that the value of the coupling coefficient decreases with temperature. The coupling coefficient reaches its peak when the grating duty cycle is 50%. The coupling coefficient increases initially as the grating depth increases, however remains almost fixed as the grating depth crosses a threshold value. Rectangular grating has a greater coupling coefficient than has trapezoidal grating. Since the coupling coefficient is a measure of the coupling between the forward and backward scattering waves, the greater its value, the selective a DFB-QCL becomes in choosing a lasing mode.

To observe the output characteristics of DFB-QCLs, we have simulated a variety of designs of DFB-QCLs. We changed the grating period, grating depth and grating shape of the waveguide and analyzed the output optical power. We used FDTD method solving the DFB-QCL waveguide structure. FDTD solutions help us to obtain the frequency solution by exploiting Fourier transforms, and thus help us to obtain full range of useful quantities, such as the electric field intensity of output emission of the QCL and associated optical power with varying wave-

length. From the analysis we found that the single mode operation of DFB-QCL can be achieved by varying the grating period, grating depth, and grating shape of the waveguide structure. For our specific structure, single-mode operation is best achieved with a rectangular grating i. e. 90° tooth angle, 1.5 μm grating period and 500 nm grating depth. For all the other designs, either the lasing output is multi-mode or the intensity of the output power is lower.

It may be argued that QCL technology now meets most of the expectations required from mid-IR sources for the targeted applications in spectroscopy, imaging, and remote-sensing. Whereas high-output power, single mode operation, self-focussing, and narrow beam-patterns have been demonstrated separately, a yet another challenge is to obtain all these characteristics simultaneously without compromising on the temperature performance. The realization of these characteristics is fulfilled only with the employment of DFB-QCLs operating in CW mode which have a single-mode, very narrow spectral linewidth and wide tuning range.

Appendix A

Simulation of DFB-QCL to evaluate the coupling coefficient

In this chapter we describe our simulation model to evaluate the coupling coefficient of a distributed feedback quantum cascade laser using MATLAB and Lumerical MODE Solutions based package.

The device being studied here is a waveguide with distributed feedback corrugation on the top cladding layer. The active layer is QCL. The top cladding layer is composed of InP and InGaAs grating. The bottom cladding layer is InGaAs on an InP substrate. We will simulate this device to calculate the coupling coefficient. As an example, we will consider 200 K temperature, 500 nm grating depth, 1.4 μm grating period, 50d% duty cycle/. The steps, in progressive order, are as follow.

A.1 Refractive Index of Active Layer

We first calculate the refractive index of the QCL using the following MATLAB code. Here, the variable, n, will give the result.

```
x_bar = 0.52; %In content in InAlAs
x_wl = 0.53; %In content in InGaAs

load Input\Maulini_APL_AI_Trial2.txt
%make a text file with 1st column the length of each layer and 2nd column
%the type of material.
C1 = Maulini_APL_AI_Trial2(:,1);
C2 = Maulini_APL_AI_Trial2(:,2);

T = 200;

n_bar = n_T_InAlAs(x_bar,T); %barrier material (InAlAs)
n_wl = n_T_InGaAs(x_wl,T); %well material (InGaAs)

len = length(C1);
sum_x = 0;
for i = 1:len
    sum_x = sum_x + C1(i);
end
P1 = 0;
P2 = 0;
for i = 1:len
    if ((C2(i)==3 || C2(i)==1))
        P1 = P1 + n_bar*C1(i);
    else
        P2 = P2 + n_wl*C1(i);
    end
end
n = (P1+P2)/sum_x
```

The function "n_T_InAlAs(x_bar,T).m" measures the refractive index of each InAlAs layer using the method described in Sec. 2.5.1 and given as follows.

```
function n = n_T_InAlAs(x,T)

EgX_AlAs = 2.239 - ((6e-4).*(T.^2)./(408+T));
EgX_InAs = 2.278 - ((5.78e-4).*(T.^2)./(83+T));
CgX = -0.713;

EgG_AlAs = 2.891 - ((8.78e-4).*(T.^2)./(332+T));
```

```
EgG_InAs = 0.42 - ((2.5e-4).*(T.^2)./(75+T));
CgG = -0.3;

for i = 1:length(x)
    EgX(i,:) = EgX_AlAs*(1-x(i)) + EgX_InAs*x(i) + CgX*(1-x(i))*x(i);
    EgG(i,:) = EgG_AlAs*(1-x(i)) + EgG_InAs*x(i) + CgG*(1-x(i))*x(i);
    Eg(i,:) = min(EgX(i,:),EgG(i,:));
    n(i,:) = 4.16 - 1.12*Eg(i,:) + 0.31*Eg(i,:).^2 - 0.08*Eg(i,:).^3;
end
end
```

The function "n_T_InGaAs(x_bar,T).m" measures the refractive index of each InGaAs layer using the method described in Sec. 2.5.1 and given as follows.

```
function n = n_T_InGaAs(x,T)

EgX_GaAs = 1.981 - ((4.6e-4).*(T.^2)./(204+T));
EgX_InAs = 2.278 - ((5.78e-4).*(T.^2)./(83+T));
CgX = -0.475;

EgG_GaAs = 1.521 - ((5.58e-4).*(T.^2)./(220+T));
EgG_InAs = 0.42 - ((2.5e-4).*(T.^2)./(75+T));
CgG = -0.475;

for i = 1:length(x)
    EgX(i,:) = EgX_GaAs*(1-x(i)) + EgX_InAs*x(i) + CgX*(1-x(i))*x(i);
    EgG(i,:) = EgG_GaAs*(1-x(i)) + EgG_InAs*x(i) + CgG*(1-x(i))*x(i);
    Eg(i,:) = min(EgX(i,:),EgG(i,:));
    n(i,:) = 4.16 - 1.12*Eg(i,:) + 0.31*Eg(i,:).^2 - 0.08*Eg(i,:).^3;
end
end
```

A.2 Refractive Index of InP

Next, we calculate the refractive index of InP layer using the method described in Sec. 2.5.2. We use the following MATLAB code to plot the refractive index vs. wavelength for two doping concentrations.

```
x = 2500:1:3500;
```

```
y = zeros(1,length(x));
z = y;
N = 5e16:5e16:2e18;
lambda = 2902.8; % wavelength in nm

for i=1:1:length(x)
    y(i) = 7.255 + (2.316*x(i)*x(i))/(x(i)*x(i)-0.392*1e6);
    y(i) = sqrt(y(i));
    z(i) = 7.194 + (2.282*x(i)*x(i))/(x(i)*x(i)-0.422*1e6);
    z(i) = sqrt(z(i));
    if x(i)==lambda
        index = i;
    end
end
plot(x,y,x,z)
```

Here, the variable, 'lambda' is found by solving the wave-functions of the QCL, and then dividing the free-space peak emission wavelength by the refractive index of the active region found in Sec. A.1. The result is shown in Fig. A.1.

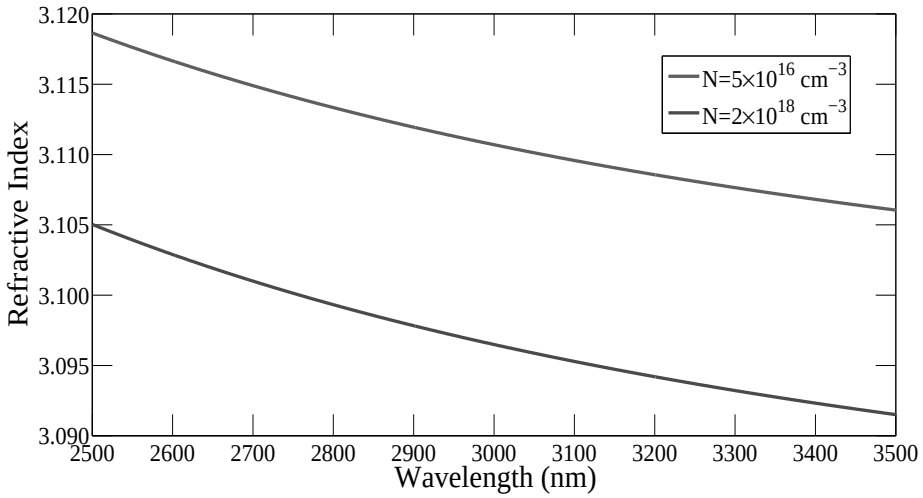

Figure A.1: Refractive Index vs. Wavelength of InP using the method described in Sec. 2.5.2.

Then using the curve fitting tool of MATLAB, we find the refractive index of InP for our desired concentration ($1 \times 10^{17} \mathrm{cm}^{-3}$).

A.3 Refractive Index of InGaAs

Using a similar method as for InP (Sec. A.2), we find the refractive index of InGaAs layer using the process mentioned in Sec. 2.5.3.

A.4 Determination of Coupling Coefficient

Now, we use Lumerical MODE Solutions to draw our desired waveguide device. We start by creating three new dielectric material with refractive indices values found in Secs. A.1, A.2, A.3 for active region, InP and InGaAs layer respectively. The physical structures to be modeled are created using the STRUCTURES tab in the Layout Editor. We draw the structure as shown in Fig. 2.4. We use the object 'Grating Coupler' with the following properties: Next we choose 'Eigenmode

Table A.1: Properties of the Grating Coupler

Property Name	**Description**	**Value**
index coating	InP layer refractive index	3.1113
index grating	InGaAs layer refractive index	3.2
n periods	No. of Grating Periods	32
tooth angle	Sloping teeth angle	90°
duty cycle	Length of each tooth divided by length of one period	0.5
period	length of each repeated structure	1.4 μm

Solver' as the Simulation Region with background index 1 and solver type '2D Z Normal'. All the boundary conditions are selected as 'PML'. After solving the eigenmodes, we get the effective refractive indices of the low and high frequency modes. The low-frequency mode is more concentrated in the higher index part of the grating and the high-frequency mode is more concentrated in the lower index

part of the grating. Then we put these values in Eq. 2.15 to find the coupling coefficient (κ). For the device structure mentioned in the Appendix, κ equals 29.15 cm^{-1}.

Appendix B

Simulation of DFB-QCL to obtain Output Optical Power

In this chapter we describe our simulation model to evaluate the output optical power of a distributed feedback quantum cascade laser using Lumerical FDTD Solutions based package. Here, we demonstrate an example of a rectangular shaped corrugated DFB-QCL with 500 nm grating depth, 1.4 μm grating period, 50% duty cycle. This is the same structure that we used to calculate the coupling coefficient in Appendix A.

We start our model by opening a blank simulation file. We first select a 'Polygon' from the 'Structures' button with the following properties for the InGaAs part of the top cladding layer:

Next, we again choose 'Polygon' from the 'Structures' button with the following properties for the InP part of the top cladding layer:

Table B.1: Properties of InGaAs top cladding layer

Tab	**Property**	**Value**
Geometry	z (μm)	0
	z span (μm)	0.5
	vertices	(0,0)
		(0.7,0)
		(0.7,0.5)
		(0,0.5)
Material	material	InGaAs

Table B.2: Properties of InP top cladding layer

Tab	**Property**	**Value**
Geometry	z (μm)	0
	z span (μm)	0.5
	vertices	(0,0.5)
		(0.7,0.5)
		(0.7,0)
		(1.4,0)
		(1.4,4.5)
		(0,4.5)
Material	material	InP

These two parts are then grouped together and work as a unit cell for the whole structure. They are copied 720 times to get a device length of 1.008 μm, which is equal to our assumed cavity length. Next, the active layer and the bottom cladding layer consisting of InP and InGaAs are drawn using 'Rectangle' from the 'STRUCTURES' menu with 1.008 μm length along x-direction. The lengths along y-direction are as mentioned in Sec. 2.4.

Next we define a FDTD simulation region with properties set according to the following table. Then we choose 'Mode' from 'Sources' and place it inside the

Table B.3: Properties of Simulation Region

Tab	**Property**	**Value**
Geometry	dimension	2D
	background index	1
	simulation time (fs)	500000
Mesh Settings	mesh accuracy	4
Boundary Conditions	x min bc, x max bc	PML
	y min bc, y max bc	PML

simulation region on the left side of the structure drawn. The source has the following properties:

Table B.4: Properties of Mode Source

Tab	**Property**	**Value**
General	injection axis	x-axis
	direction	Forward
	mode selection	fundamental TE mode
Frequency/Wavelength	wavelength start (μm)	8.65
	wavelength stop (μm)	9.35

Lastly, we choose 'Frequency-domain field profile' from 'MONITORS' that has the following properties. The monitor is placed on the right wall of the structure so that the emitted radiations from the source pass through the DFB, reflects inside the cavity several times and we note the emitted radiation from the right side of our drawn structure.

Table B.5: Properties of the Monitor

Tab	**Property**	**Value**
General	simulation type	2D Z-normal
	use source limits	Yes
	frequency points	500
Data to record	standard fourier transform	Yes
	Fields	Ex, Ey, Ez, Hx, Hy, Hz
	Poynting vector and power	output power

After running the simulation, we get the result. We choose Visualizer from the Monitor and select 'P' to observe the output power and get the result shown in Fig. 3.6.

Bibliography

[1] S. W. Sharpe, T. J. Johnson, R. L. Sams, P. M. Chu, G. C. Rhoderick, and P. A. Johnson, "Gas-Phase Databases for Quantitative Infrared Spectroscopy," *Applied Spectroscopy*, vol. 58, no. 12, pp. 1452–1461, 2004.

[2] C. H. Townes, *A Century of Nature: Twenty-One Discoveries that Changed Science and the World*. University of Chicago Press, 2008.

[3] H. C. Liu, "A Novel Superlattice Infrared Source," *Journal of Applied Physics*, vol. 63, p. 2856, 1988.

[4] Z. I. Alferov, "The History and Future of Semiconductor Heterostructures," *Semiconductors*, vol. 32, no. 1, pp. 1–14, 1998.

[5] J. Faist, F. Capasso, D. L. Sivco, C. Sirtori, A. L. Hutchinson, and A. Y. Cho, "Quantum Cascade Laser," *Science*, vol. 264, pp. 553–556, 1994.

[6] J. Hodgkinson and R. P. Tatam, "Optical Gas Sensing: A Review," *Measurement Science and Technology*, vol. 24, pp. 012 004(1)–012 004(59), 2013.

[7] A. Yariv, *Quantum Electronics*, 3rd ed. John Wiley & Sons Ltd., 1989.

[8] C. Sirtori and R. Teissier, *Intersubband Transitions in Quantum Structures*, R. Paiella, Ed. McGraw Hill, 2006.

[9] Q. Y. Lu, Y. Bai, N. Bandyopadhyay, S. Slivken, and M. Razeghi, "2.4 W Room Temperature Continuous Wave Operation of Distributed Feedback Quantum Cascade Lasers," *Appl. Phys. Lett.*, vol. 98, pp. 181 106(1)–181 106(3), 2011.

[10] C. Gmachl, A. Straub, R. Colombelli, F. Capasso, D. L. Sivco, A. M. Sergent, and A. Y. Cho, "Single-mode, Tunable Distributed-feedback and Multiple-wavelength Quantum Cascade Lasers," *IEEE Journal of Quantum Electronics*, vol. 38, no. 6, pp. 569–581, 2002.

[11] A. Wittmann, Y. Bonetti, M. Fischer, J. Faist, S. Blaser, and E. Gini, "Distributed-Feedback Quantum-Cascade Lasers at 9 m Operating in Continuous Wave Up to 423 K," *IEEE Photonics Technology Letters*, vol. 21, no. 12, pp. 814–816, 2009.

[12] Z. Jinchuan, W. Lijun, L. Wanfeng, L. Fengqi, Z. Lihua, Z. Shenqiang, L. Junqi, and W. Zhanguo, "Distributed Feedback Quantum Cascade Lasers Operating in Continuous-Wave Mode at =7.6 m," *Journal of Semiconductors*, vol. 33, no. 2, pp. 024 005(1)–024 005(3), 2012.

[13] J. M. Wolf, A. Bismuto, M. Beck, and J. Faist, "Distributed-Feedback Quantum Cascade Laser Emitting at 3.2 m." Munich, Germany: The European Conference on Lasers and Electro-Optics, 2014.

[14] M. Beck, D. Hofstetter, T. Aellen, J. Faist, U. Oesterle, M. Ilegems, E. Gini, and H. Melchior, "Continuous Wave Operation of a Mid-Infrared Semiconductor Laser at Room Temperature," *Science*, vol. 295, p. 301, 2002.

[15] A. Evans, J. S. Yu, J. David, L. Doris, K. Mi, S. Slivken, and M. Razeghi, "High-temperature, High-power, Continuous-wave Operation of Buried Heterostructure Quantum-cascade Lasers," *Appl. Phys. Lett.*, vol. 84, p. 314, 2004.

[16] A. A. Kosterev, R. F. Curl, F. K. Tittel, M. Rochat, M. Beck, D. Hofstetter, and J. Faist, "Chemical sensing with pulsed QC-DFB lasers operating at 15.6 m," *Applied Physics B*, vol. 75, no. 2-3, pp. 351–357, 2002.

[17] J. S. Yu, S. Slivken, S. R. Darvish, A. Evans, B. Gokden, and M. Razeghi, "High-power, room-temperature, and continuous-wave operation of distributed-feedback quantum-cascade lasers at 4.8 m," *Appl. Phys. Lett.*, vol. 87, pp. 041 104(1)–041 104(3), 2005.

[18] W. Zeller, L. Naehle, P. Fuchs, F. Gerschuetz, L. Hildebrandt, and J. Koeth, "DFB Lasers Between 760 nm and 16 m for Sensing Applications," *Sensors*, vol. 10, pp. 2492–2510, 2010.

[19] O. Cathabard, R. Teissier, J. Devenson, and A. N. Baranov, "InAs-based Distributed Feedback Quantum Cascade Lasers," *Electronics Letters*, vol. 45, no. 20, pp. 1028–1030, 2009.

[20] S. Welzel, F. Hempel, M. Hbner, N. Lang, P. B. Davies, and J. Rpcke, "Quantum Cascade Laser Absorption Spectroscopy as a Plasma Diagnostic Tool: An Overview," *Sensors*, vol. 10, pp. 6861–6900, 2010.

[21] R. F. Curl, F. Capasso, C. Gmachl, A. A. Kosterev, B. McManus, R. Lewicki, M. Pusharsky, G. Wysocki, and F. K. Tittel, "Quantum Cascade Lasers in Chemical Physics," *Chemical Physics Letters*, vol. 487, pp. 1–10, 2010.

[22] Y. Ma, R. Lewicki, M. Razeghi, and F. K. Tittel, "QEPAS based ppb-level detection of CO and N2O using a high power CW DFB-QCL," *Opt. Express*, vol. 13, no. 1, pp. 1008–1019, 2013.

[23] J. P. Waclawek, R. Lewicki, H. Moser, M. Brandstetter, F. K. Tittel, and B. Lendl, "Sulfur Dioxide Detection Using CW-DFB-QCL Based Quartz-Enhanced Photoacoustic Spectroscopy." San Jose, California, United States: CLEO: Applications and Technology, June 2013.

[24] R. Bartlome, A. Feltrin, and C. Ballif, "Infrared Laser-based Monitoring of the Silane Dissociation during Deposition of Silicon Thin Films," *Appl. Phys. Lett.*, vol. 94, p. 201501, 2009.

[25] B. G. Lee, M. A. Belkin, C. Pflugl, L. Diehl, H. A. Zhang, R. M. Audet, J. MacArthur, D. P. Bour, S. W. Corzine, G. E. Hofler, and F. Capasso, "DFB Quantum Cascade Laser Arrays," *IEEE Journal of Quantum Electronics*, vol. 45, no. 5, pp. 554–565, 2009.

[26] B. G. Lee, "Beam Combining of Quantum Cascade Laser Arrays," *Opt. Express*, vol. 17, p. 16216, 2009.

[27] H. Kogelnik and C. V. Shank, "Coupled Wave Theory of Distributed Feedback Lasers," *J. Appl. Phys.*, vol. 43, pp. 2327–2335, 1972.

[28] W. Streifer, R. D. Burnham, and D. R. Scifres, "Effect of External Reflectors on Longitudinal Modes of Distributed Feedback Lasers," *IEEE Journal of Quantum Electronics*, vol. QE-11, no. 4, pp. 154–161, 1975.

[29] P. Correc, "Coupling Coefficients for Trapezoidal Gratings," *IEEE Journal of Quantum Electronics*, vol. QE-24, no. 1, pp. 8–10, 1988.

[30] J. Faist, C. Gmachl, F. Capasso, C. Sirtori, D. L. Sivco, J. N. Baillargeon, and A. Y. Cho, "Distributed Feedback Quantum Cascade Lasers," *Appl. Phys. Lett.*, vol. 70, pp. 2670–2672, 1997.

[31] K. S. Yee, "Numerical Solution of Initial Boundary Value Problems involving Maxwells Equations in Isotropic Media," *IEEE Transactions on Antennas and Propagation*, vol. 14, pp. 302–307, 1966.

[32] D. M. Sullivan, *Electromagnetic Simulation Using the FDTD Method*. New York: IEEE Press Series, 2000.

[33] A. Taflove, *Computational Electromagnetics: The Finite-Difference Time-Domain Method*. Boston: Artech House, 2005.

[34] S. D. Gedney, *Introduction to the Finite-Difference Time-Domain (FDTD) Method for Electromagnetics*. Morgan & Claypool publishers, 2011.

[35] H. Kogelnik, "Coupled Wave Theory for a Thick Hologram Grating," *Bell Syst. Tech. J.*, vol. 48, pp. 2909–2947, 1969.

[36] S. Wang, "Principles of Distributed Feedback and Distributed Bragg Reflector Lasers," *IEEE Journal of Quantum Electronics*, vol. QE-10, no. 4, pp. 413–427, 1974.

[37] A. Yariv and A. Gower, "Equivalent of the Coupled Mode and Floquet-Bloch Formalism in Periodic Optical Waveguide," *Appl. Phys. Lett.*, vol. 26, pp. 537–539, 1975.

[38] K. David, J. Buus, and R. Baets, "Basic Analysis of AR-coated, Partly Gain-coupled DFB Lasers: The Standing Wave Effect ," *IEEE Journal of Quantum Electronics*, vol. 28, no. 2, pp. 427–433, 1992.

[39] J. Faist, D. Hofstetter, M. Beck, T. Aellen, M. Rochat, and S. Blaser, "Bound-to-Continuum and Two-Phonon Resonance Quantum-Cascade Lasers for High Duty Cycle, High-Temperature Operation," *IEEE Journal of Quantum Electronics*, vol. 38, no. 6, pp. 533–546, 2002.

[40] R. Maulini, M. Beck, and J. Faist, "Broadband Tuning of External Cavity Bound-to-Continuum Quantum-Cascade Lasers," *Appl. Phys. Lett.*, vol. 84, no. 10, pp. 1659–1661, 2004.

[41] H. Ghafouri-Shiraz, *Distributed Feedback Laser Diodes and Optical Tunable Filters*. John Wiley & Sons Ltd., 2003.

[42] Y. Luo, Y. Nakano, K. Ikeda, T. Inoue, H. Hosomatsu, and H. Iwaoka, "Low Threshold CW Operation in a Novel Gain-coupled Distributed Feedback Semiconductor Laser." Davos, Switzerland: Tech. Dig. 12th IEEE Int. Semiconductor Laser Conf., 1990, pp. 70–71.

[43] K. David, G. Morthier, P. Vankwikelberge, and R. Baets, "Partly Gain-coupled versus /4-shifted-DFB Laser: A Comparison." Davos, Switzerland: Tech. Dig. 12th IEEE Int. Semiconductor Laser Conf., 1990, pp. 202–203.

[44] K. Petermann, *Laser Diode Modulation and Noise*. Tokyo, Japan: KTK Scientific and Kluwer Academic Publishers, 1988.

[45] H. Temkin, R. A. Logan, N. A. Olsson, C. H. Henry, G. J. Dolan, R. F.

Kazarinov, and L. F. Johnson, "InGaAsP Ridge Waveguide Distributed Feedback Lasers Operating near 1.55 m," *J. Lightwave Technol.*, vol. LT-4, pp. 520–529, 1986.

[46] V. P. Gupta and N. M. Ravindra, "Energy Gap-Refractive Index Relations in Semiconductors - An Overview," *Physica Status Solidi*, vol. 100, pp. 715–719, 1980.

[47] D. Penn, "Wave-Number-Dependent Dielectric Function of Semiconductors," *Physical Review Letters*, vol. 128, pp. 2093–2097, 1962.

[48] Y. Varshni, "Temperature Dependence of the Energy Gap in Semiconductors," *Physica*, vol. 34, pp. 149–154, 1967.

[49] B. Nag, *Electron Transport in Compound Semiconductors*. Springer Series in Solid-State Sciences, 1980, vol. 11.

[50] S. Adachi, "GaAs, AlAs, and AlGaAs: Material Parameters for Use in Research and Device Applications," *Journal of Applied Physics*, vol. 58, pp. R1–R29, 1985.

[51] J. Singh, *Physics of Semiconductors and their Heterostructures*. McGraw Hill, 1993.

[52] S. Tiwari, *Compound Semiconductor Device Physics*. Academic Press, 1992.

[53] G. D. Pettit and W. J. Turner, "Refractive index of inp," *Journal of Applied Physics*, vol. 36, p. 2081, 1965.

[54] M. S. Whalen and J. Stone, "Index of Refraction of n-type InP at 0.633 and 1.15 m Wavelengths as a Function of Carrier Concentration," *Journal of Applied Physics*, vol. 53, p. 4340, 1982.

[55] P. Martin, E. M. Skouri, L. Chusseau, C. Alibert, and H. Bissessur, "Accurate Refractive Index Measurements of Doped and Undoped InP by a Grating Coupling Technique," *Appl. Phys. Lett.*, vol. 67, no. 7, pp. 881–883, 1995.

[56] S. Gozu, T. Mozume, and H. Ishikawa, "Refractive Index of Si-doped n-InGaAs," *Journal of Applied Physics*, vol. 104, pp. 073 507(1)–073 507(4), 2008.

[57] R. Millett, K. Hinzer, T. Hall, and H. Schriemer, "Optimal Cavity Lengths and Duty Cycles for Second-order Laterally-coupled Distributed Feedback Lasers." Ottawa, Canada: Microsystems and Nanoelectronics Research Conference, 2008, pp. 61–64.

[58] A. Sadeghi, P. Q. Liu, X. Wang, J. Fan, M. Troccoli, and C. F. Gmachl, "Wavelength Selection and Spectral Narrowing of Distributed Bragg Reflector Quantum Cascade Lasers up to Peak Optical Power," *Opt. Express*, vol. 21, pp. 31 012–31 018, 2013.

[59] J. Li and J. Cheng, "Laterally-coupled Distributed Feedback Laser with First-order Gratings by Interference Lithography," *Electronics Letters*, vol. 49, no. 12, pp. 764–766, 2013.

[60] V. V. Vasileva, D. A. Vinokurov, V. V. Zolotarev, A. Y. Leshko, A. N. Petrunov, N. A. Pikhtin, M. G. Rastegaeva, Z. N. Sokolova, I. S. Shashkin,

and I. S. Tarasov, “High-order Diffraction Gratings for High-power Semiconductor Lasers,” *Semiconductors*, vol. 46, no. 2, pp. 241–246, 2012.

[61] H. Ghafouri-Shiraz and B. S. K. Lo, “Computation of Coupling Coefficient for a Five-layer Trapezoidal Grating Structure,” *Opt. and Laser Technol.*, vol. 27, no. 1, pp. 45–48, 1994.

[62] P. Bhattacharya, *Semiconductor Optoelectronic Devices*. Prentice-Hall of India, 2002.

[63] S. O. Kasap, *Optoelectronics And Photonics: Principles and Practices*. Pearson Education, 2001.

[64] J. Faist, F. Capasso, C. Sirtori, D. L. Sivco, and A. Y. Cho, *Intersubband Transitions In Quantum Wells: Physics and Device Applications II*, H. C. Liu and F. Capasso, Eds. Academic Press, 2000, vol. 66.

[65] R. Ferreira and G. Bastard, “Evaluation of Some Scattering Times for Electrons in Unbiased and Biased Single- and Multiple-quantum-well Structures,” *Phys. Rev. B*, vol. 40, pp. 1074–1086, 1989.

[66] T. Unuma, M. Yoshita, T. Noda, H. Sakaki, and H. Akiyama, “Intersubband Absorption Linewidth in GaAs Quantum Wells due to Scattering by Interface Roughness, Phonons, Alloy Disorder, and Impurities,” *J. Appl. Phys.*, vol. 93, pp. 1586–1597, 2003.

[67] A. Wittmann, Y. Bonetti, J. Faist, E. Gini, and M. Giovannini, “Intersubband Linewidths in Quantum Cascade Laser Designs,” *Appl. Phys. Lett.*, vol. 93, 2008.

[68] D. Indjin, P. Harrison, R. W. Kelsall, and Z. Ikonic, "Self-consistent Scattering Theory of Transport and Output Characteristics of Quantum Cascade Lasers," *J. Appl. Phys.*, vol. 91, pp. 9019–9026, 2002.

[69] M. R. Salehi and B. Cabon, "Circuit Modeling of Quantum-Well Lasers for Optoelectronic Integrated Circuits (ICs) Including Physical Effect of Deep-Level Traps," *IEEE Journal of Quantum Electronics*, vol. 38, no. 11, pp. 1510–1514, 2002.

[70] J. P. Berenger, "A Perfectly Matched Layer for the Absorption of Electromagnetic Waves," *Journal of Computational Physics*, vol. 114, no. 2, pp. 185–200, 1994.

[71] K. Namjou, S. Cai, E. A. Whittaker, J. Faist, C. Gmachl, F. Capasso, D. L. Sivco, and A. Y. Cho, "Sensitive Absorption Spectroscopy with a Room-temperature Distributed-Feedback Quantum-Cascade Laser," *Optics Letters*, vol. 23, no. 3, pp. 219–221, 1998.

[72] A. Zakery, R. Zare, and A. Bakhtazad, "Coupled Mode Analysis of Second Order Loss-coupled DFB Lasers," in *Semiconductor Lasers II*, vol. 75. Beijing, China: Proc. SPIE 2886, 1996.